AIAA JOURNAL
Vol. 63, No. 11, November 2025

Generalized Similarity Laws for Unstart Phenomenon of Contraction Ducts in Supersonic Flow

Xiao-tong Tong*
Peking University, 100871 Beijing, People's Republic of China
Qi-fan Zhang,† Wan-nan Wu,† Lian-jie Yue,‡ and Cheng-ming He§
Institute of Mechanics, Chinese Academy of Sciences, 100190 Beijing, People's Republic of China
and
Zheng Chen¶
Peking University, 100871 Beijing, People's Republic of China

https://doi.org/10.2514/1.J065313

The prediction of hypersonic inlet unstart has been a difficult aerodynamic problem over the past half century. Different from inviscid unstart theories, this study develops empirical and theoretical prediction methods for viscous flow. By proposing a corrected contraction angle and contraction ratio, a generalized similarity law for unstart boundary is established and validated by sufficient numerical and experimental results, describing the effects of aerodynamic and geometric parameters simultaneously. To explain the physical implications of the generalized unstart similarity law, two-dimensional flow-based theoretical models are established for three unstart modes using oblique shock relations, free interaction theory, and scaling laws for separation length. For the short-cowl and long-cowl modes, the self-similarity of the unstart boundary is attributed to the separation scale relative to the effective throat height and the mass-averaged throat Mach number accompanied by shock reflections, respectively. The transitional unstart is triggered by the decrease of the shock-impingement distance relative to the separation scale, and the self-similarity is broken by the wedge length independence and Reynolds number dependence. Moreover, to facilitate unstart detection in wind tunnel or flight tests, the corrected dimensionless pressure rise is proposed, correlating the critical wall pressure characteristics with the incident shock pressure rise and dimensionless wedge length.

Nomenclature

A	=	correction factor
B	=	correction factor
b	=	empirical parameter
C_f	=	coefficient of wall friction
d	=	empirical parameter
h_c	=	cowl lip height, mm
h_t	=	geometric throat height, mm
i	=	reference number of shock initiation points
ICR	=	internal contraction ratio
ICR_{eff}	=	effective internal contraction ratio
ICR_{effM}	=	corrected internal contraction ratio
L_c	=	cowl length, mm
L_c	=	dimensionless cowl length
L_f	=	length of upstream plate, mm
L_i	=	length of shock wave, mm
$L_{i,i+2}$	=	shock impingement spacing, mm
L_{sep}	=	separation length, mm
M	=	Mach number
n_t	=	total number of shock initiation points
p	=	static pressure, kPa
$p_{\text{max-un}}$	=	critical wall pressure peak, kPa
Re	=	Reynolds number
S	=	area, m^2
T	=	temperature, K
u	=	velocity, m/s
x	=	X-coordinate, mm
α	=	empirical parameter
β	=	shock angle, deg
γ	=	specific heat ratio
δ_c	=	entrance boundary-layer thickness, mm
δ_c^*	=	entrance displace thickness, mm
θ_c	=	contraction angle, degree
θ_{cM}	=	corrected contraction angle, deg
μ	=	dynamic viscosity, $\text{kg/m} \cdot \text{s}$
ρ	=	density, kg/m^3

Subscripts

c	=	value at the cowl lip position
eff	=	effective quantity
max	=	pressure peak
un	=	unstart boundary
unc	=	unstart critical state
uncM	=	corrected critical value
s	=	value of separation shock
t	=	value at the throat
0	=	reference value
1, 2, ...	=	reference number of shock initiation point
∞	=	freestream condition

Received 7 January 2025; accepted for publication 6 April 2025; published online 11 June 2025.

*Postdoctoral Researcher, College of Engineering.
†Associate Professor, State Key Laboratory of High-Temperature Gas Dynamics.
‡Professor, State Key Laboratory of High-Temperature Gas Dynamics; also University of Chinese Academy of Sciences, 100049 Beijing, People's Republic of China; yuelj@imech.ac.cn (Corresponding Author).
§Professor, State Key Laboratory of High-Temperature Gas Dynamics; chengming.he@ujs.edu.cn (Co-Corresponding Author).
¶Professor, College of Engineering.

I. Introduction

THE supersonic flow characteristics in contraction ducts [1], as a classic problem in aerodynamics, are significant to ramjets (Fig. 1a) [2–4], oblique detonation engines [5–8], supersonic wind tunnel diffusers [9–11], and turbomachinery [12]. The supersonic contraction duct or diffuser has two operating states: the started state (Fig. 1b) and the unstarted state (Fig. 1c). In the started state, the

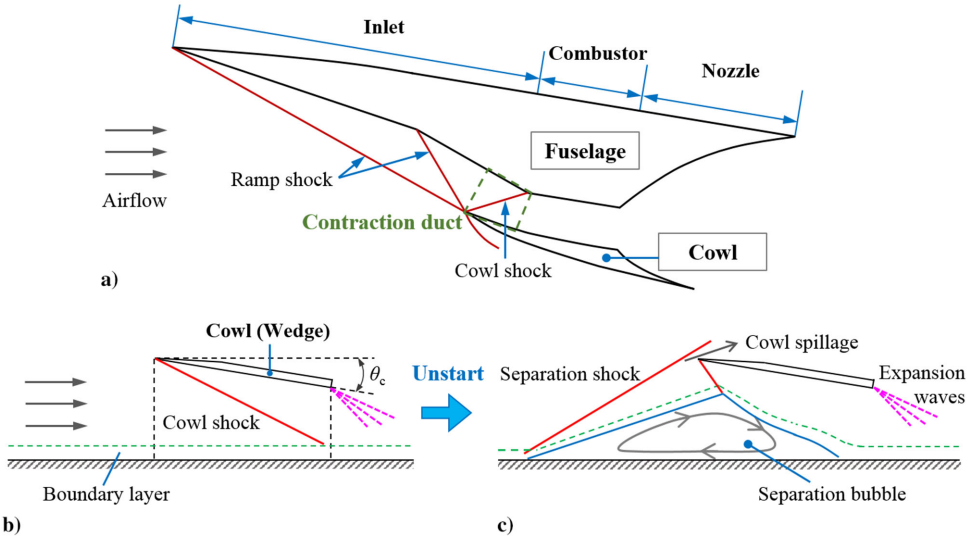

Fig. 1 Flow regimes of contraction ducts: a) schematic of a hypersonic airbreathing vehicle, b) started state, and c) unstarted state.

airflow capture characteristics at the entrance are not affected by the downstream internal flow [4]. In the unstarted state, the airflow capture and total pressure recovery decrease, and shock oscillation occurs. With the growing concern over hypersonic airbreathing propulsion [2,3,13], recent research on supersonic converging duct flows has mainly focused on hypersonic inlets [14,15]. Figure 1a shows a typical hypersonic inlet lying between the fuselage and the cowl. As a key component of the propulsion system, the hypersonic inlet captures and compresses air, which is then delivered to the downstream combustor. The unstart phenomenon of the inlets is accompanied by a catastrophic growth of the flow separation region in the contraction duct, which can significantly reduce engine thrust, increase thermal loads, worsen aircraft robustness, and even lead to flight failure. Therefore, accurate prediction of the unstart boundary is crucial to the design and control of hypersonic airbreathing engines.

Theoretical and empirical investigations on the unstart boundary of hypersonic inlets date back to the 1960s. Based on the one-dimensional and inviscid flow assumptions, classical theories provided the isentropic limit and Kantrowitz limit [16,17], which were regarded as the unstart boundary and restart boundary, respectively. The corresponding curves are shown in Fig. 2. The isentropic theory assumes that the airflow is isentropically compressed in the contraction duct and experiences choking at the geometric throat, leading to unstart. The following formula can be derived:

$$\left(\frac{S_c}{S_t}\right)_{\text{Isentropic}} = \frac{1}{M_\infty}\left(\frac{2}{\gamma+1}+\frac{\gamma-1}{\gamma+1}M_\infty^2\right)^{\frac{\gamma+1}{2(\gamma-1)}} \tag{1}$$

where S_c and S_t are the entrance area and throat area of the contraction duct, respectively. The entrance/throat area ratio is known as the internal contraction ratio (ICR). Van Wie [4] obtained an empirical formula of unstart area ratio about entrance Mach number M_∞ by data fitting:

$$\left(\frac{S_t}{S_c}\right)_{\text{un}} = 0.05 - \frac{0.52}{M_\infty} + \frac{3.65}{M_\infty^2}, \qquad 2.5 < M_\infty < 10 \tag{2}$$

In Fig. 2, this formula is close to the isentropic limit.

According to Kantrowitz [16], a normal shock is assumed to stand at the entrance when start occurs. The gas accelerates isentropically to $M = 1$ in the internal duct, and the restart area ratio can be obtained:

$$\left(\frac{S_c}{S_t}\right)_{\text{Kantrowitz}} = \sqrt{\frac{\gamma+1}{2+(\gamma-1)M_\infty^2}}\cdot M_\infty^{\frac{\gamma+1}{\gamma-1}}\cdot\left(\frac{2\gamma}{\gamma+1}M_\infty^2-\frac{\gamma-1}{\gamma+1}\right)^{\frac{1}{1-\gamma}} \tag{3}$$

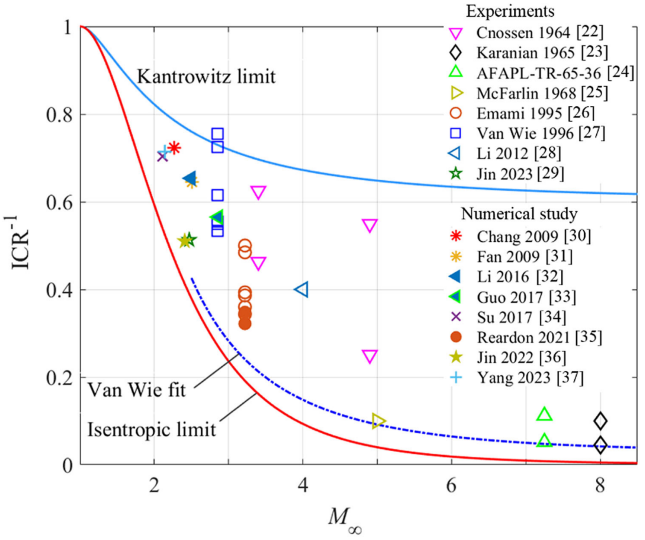

Fig. 2 Unstart boundaries in the literature [22–37] compared to theoretical and empirical equations.

Subsequent researchers extend Kantrowitz's theory in an inviscid framework, considering the external compression shocks and curved compression surface [17–20]. The empirically corrected Kantrowitz limit is still used in the prediction of ODE unstart [7], where the boundary-layer separation structure is oversimplified into a Mach stem, and the multiple reflections of the incident wave are ignored. Moreover, the unstart/restart boundaries are generally unequal because of the unstart/restart hysteresis [21]. The derivatives of the Kantrowitz limit are suitable to restart the boundary rather than unstart the boundary. Hence, further modifications to the aged Kantrowitz theory seems unphysical and unpromising.

In Fig. 2, the unstart boundaries obtained by experiments and numerical simulation [22–37] are highly discrete, and neither theoretical nor empirical formulas give accurate predictions. Though there are overlapping symbols, they don't represent data collapse or self-similarity. This is attributed to the shock-wave/boundary-layer interaction (SWBLI) in actual inlets [38]. The cowl shock intensity, varying with the contraction angle, influences the boundary-layer separation flow significantly [26,27,39,40]. However, the effect of contraction angle is ignored by Eqs. (1–3). Additionally, viscous effect is also considerable. Even if the incident shock intensity is

fixed, the unstart contraction ratios are still discrete for varying Reynolds numbers or entrance boundary-layer characteristics.

Due to the complexity of turbulent SWBLI, there has been no complete theoretical model for the scale and dynamic behavior of the boundary-layer separation region under the influences of multiple variables. Hence, it is difficult to directly determine the trigger for the catastrophic growth of the separation region from first principles of fluid mechanics. Existing literature on the unstart boundary is primarily based on empirical study. Emami [26] observed in experiments that the unstart contraction angle is almost unaffected by the cowl length within a certain range. Van Wie [27] determined the unstart boundary of a contraction duct by rotating the cowl plate and proposed a concept of hard/soft unstart, suggesting that the hard unstart corresponds to relatively short cowl and high lip cases, while the soft unstart is the opposite. Other literature reported unstart caused by changes in Mach number [30–32,34], contraction angle [35,41], angle of attack [33,42], and throat height [29,36]. However, they only provide phenomenon descriptions and qualitative trends within limited parameter ranges.

Existing studies correlated the unstart boundary to dimensionless variables such as ICR, the ratio of cowl length to entrance height [26]/throat height [27]/boundary-layer thickness [39], the ratio of cowl lip height to boundary-layer thickness [39,40], and the entrance mass-averaged Mach number [22,27]. However, these variables depend on model scale (Reynolds number) and are not self-similar. Recent attempts in theoretical construction are also limited by this issue. Yang [37] developed a rapid prediction method for unstart Mach number. However, the Reynolds number was not considered, and the unstart triggering conditions are oversimplified, restricting the prediction accuracy over a wide range of aerodynamic and geometric parameters. In recent years, researchers have utilized machine learning methods in unstart detection and identification [43,44]. But machine learning methods have not yet been practical for the rapid prediction of unstart boundaries because of the high cost of systematic training samples.

In order to develop a universal prediction method for the unstart boundary, researchers have introduced the similarity analysis (dimensional analysis) method. Chang [45] used dimensional analysis to preliminarily investigate the influencing factors of the unstart boundary but did not consider the impact of inlet configuration. Tong [46] conducted systematic numerical simulations based on Van Wie's experimental model [27], dividing unstart into three modes. Two key similarity parameters were proposed: the dimensionless cowl length and the effective internal contraction ratio, and an empirical formula was developed to simultaneously describe the effects of multiple variables. However, this study incorporated the influence of Mach number into the empirical formula through direct data fitting, lacking clear physical implications.

In this study, the unstart characteristics of simplified two-dimensional contraction ducts are numerically studied. By constructing new similarity parameters, the similarity law for unstart boundary is extended, and a physical interpretation of the similarity law is provided using simplified theoretical models considering the critical separation scale and shock wave reflections in a contraction duct. This study can provide some basic principles for the design of hypersonic airbreathing engines and a new viewpoint of SWBLI scaling laws.

II. Physical Model and Numerical Method

A. Simplified Contraction Duct

The physical model and numerical methods follow the previous studies [46,47]. As shown in Fig. 3, the computational domain is a two-dimensional rectangular region between two parallel walls. The cowl (wedge plate) and the lower horizontal wall form a simplified contraction duct, which corresponds to the internal contraction passage of the inlet in Fig. 1a. Supersonic flow enters the computational domain from the left, and the height of the computational domain is more than twice the maximum entrance height of the contraction duct so that the blockage in the computational domain is avoided, as well as the interference of the reflected waves from the upper wall.

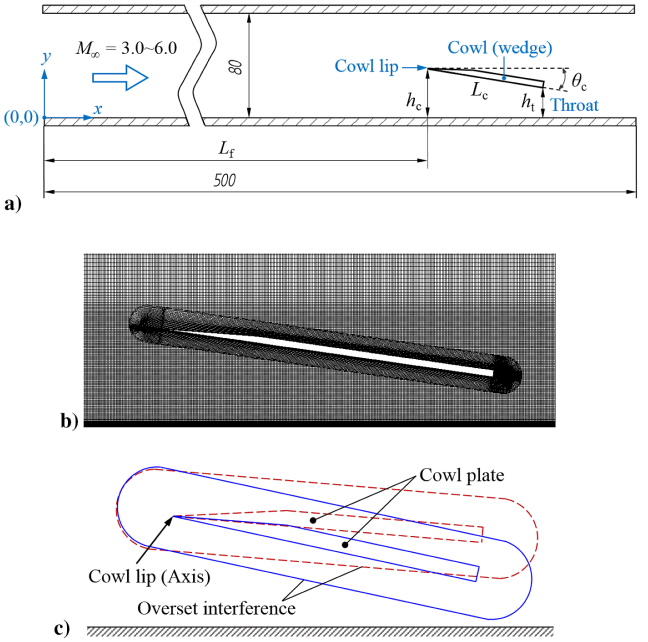

Fig. 3 Physical model: a) computational domain, b) local grid around cowl, and c) schematic of cowl rotation.

Table 1 Boundary-layer characteristics at the entrance under different conditions

No.	M_∞	p_∞, kPa	Re_{xc}, 10^7	δ_c, mm	δ_c^*, mm
1	3.0	18.77	1.433	4.82	1.52
2	3.0	9	0.687	5.10	1.57
3	3.0	30	2.290	4.60	1.25
4	4.0	18.77	1.910	4.61	1.66
5	5.0	18.77	2.388	4.38	1.91
6	6.0	18.77	2.967	4.11	2.15

Geometric parameters are labeled in Fig. 3a. The angle between the cowl and the x-axis is the cowl angle θ_c. As shown in Fig. 3b, the grid is generated using the overset grid method (commonly used in the field of aerodynamics [48]), which consists of the background and the region surrounding the cowl. The first-layer cells near the wall have a height of 0.001 mm to ensure that the $y+$ of the entire lower wall is less than 1. During the calculation, the cowl can rotate around its leading edge to adjust the ICR, as shown in Fig. 3c, where the red/blue lines denote pre/post rotation configuration. The airflow capture area of the contraction duct remains unchanged during the cowl rotation process in the started state, leading to a fixed mass flow rate. The cowl length (wedge length) L_c ranges from 12.7 to 101.6 mm, and the cowl lip height h_c ranges from 7.62 to 30.48 mm. The upstream flat plate length L_f is fixed at 279.4 mm.

The boundary-layer characteristics under different conditions are listed in Table 1. The static temperature is 107.7 K. The characteristic scale for the Reynolds number Re_{xc} is the upstream plate length L_f. In our previous work [46], the boundary-layer thickness was verified with experimental data. At Mach 3, the entrance boundary-layer thickness and Re_{xc} vary with the incoming static pressure. For a given flow condition, with L_c fixed, the unstart boundaries are sought at different h_c, and then different L_c are examined in the same manner. There are 136 groups of simulation cases in total with various combinations of L_c and h_c. Please note that L_c and h_c are fixed when adjusting θ_c in each group.

B. Numerical Method

The finite volume method is used to solve the two-dimensional Reynolds-averaged Navier–Stokes equations, based on the second-order total variation diminishing (TVD) scheme with the Harten–Lax–van Leer–Contact (HLLC) Riemann solver. This method is

widely used in hypersonic aerodynamic research. The time integration adopts the implicit dual time-stepping method for unsteady simulations, with a time step size of 1e−06 s. The maximum number of inner iterations per time step is set to 50 to ensure that the residual reduces below 1e−05. Referring to existing studies [36,40,49], the turbulence calculation employs the $k-\omega$ shear stress transport (SST) model and solves-to-wall strategy to ensure the accuracy of SWBLI calculations. All walls are adiabatic.

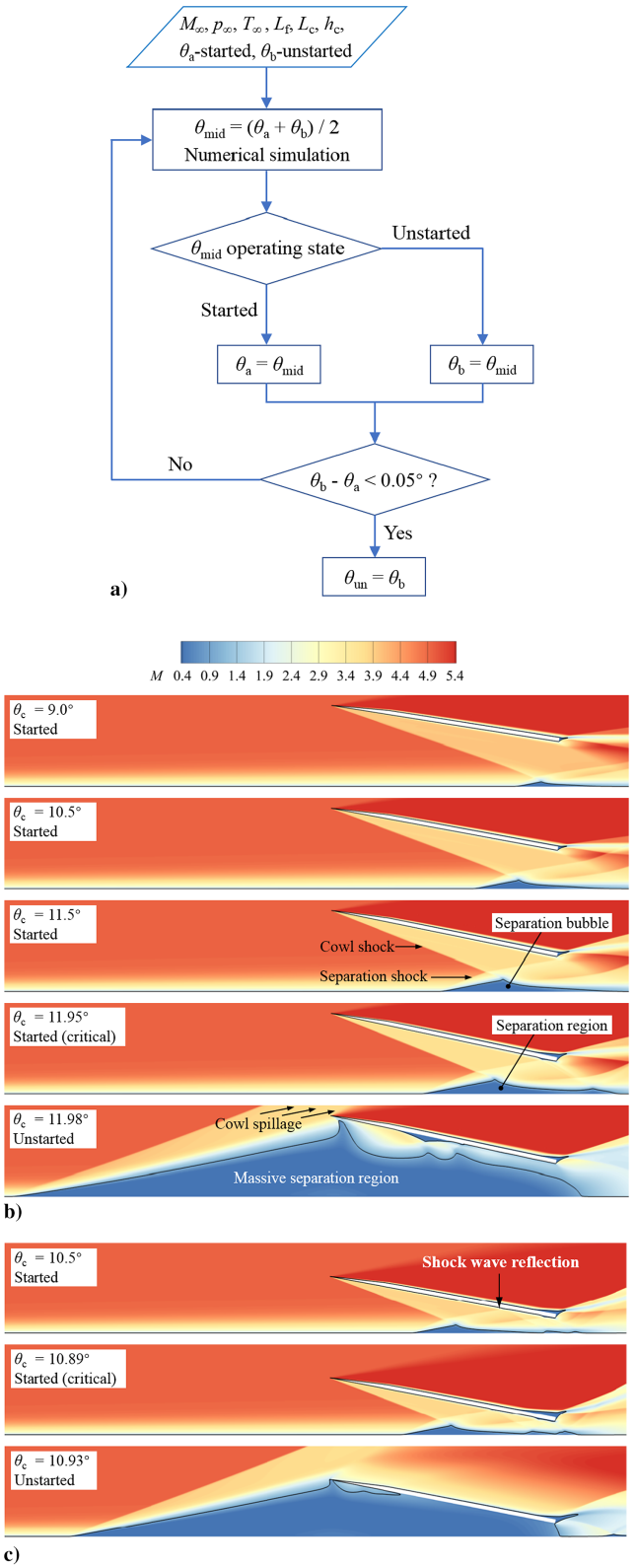

Fig. 4 Determination of unstart boundary: a) flowchart; b) flowfield at different contraction angles ($M_\infty = 5$, $L_c = 50.8$ mm, $h_c = 17.78$ mm), black lines denote the sonic position; c) flowfield at different contraction angles ($M_\infty = 5$, $L_c = 50.8$ mm, $h_c = 12.7$ mm).

At the initial moment, the throat height h_t is large enough to ensure that the initial state is started. The rotation of the cowl is achieved by updating the grid. First, the flowfield is calculated to convergence and saved for a given cowl angle, then a new grid with a larger cowl angle is generated and replaces the existing grid, and sufficient time steps are performed on the basis of the saved flowfield. Repeat this operation until the contraction duct unstarts. The cowl rotation process is quasi-steady, with each angle change not exceeding 0.05°, thus eliminating the unsteady effects of cowl rotation on unstart.

As shown in Fig. 4a, the bisection method is used to determine the unstart boundary. Firstly, the initial values of the contraction angles θ_a and θ_b are given, corresponding to the started and unstarted states, respectively. Then, numerical simulations are carried out to detect the flow state at the interval midpoint $\theta_{mid} = (\theta_a + \theta_b)/2$. If θ_{mid} is unstarted, θ_{mid} is assigned to θ_b. Otherwise, it is assigned to θ_a. In this way, the rotation step size is continuously reduced, and the unstart boundary θ_{un} can be determined with an accuracy of 0.05°.

The determination of the unstart boundary is demonstrated under No. 5 inflow condition, and the flowfields at different contraction angles are shown in Fig. 4b. As θ_c increases, the cowl shock strengthens, making the induced separation region on the lower wall grow. When θ_c increases to 11.98°, the separation region suddenly enlarges, and the airflow between the separation shock and the cowl lip no longer enters the internal duct, resulting in cowl lip spillage. Cowl spillage marks the unstarted flowfield, and thus $\theta_c = 11.98°$ is the unstart boundary. The state where θ_c is very close to the unstart boundary before unstart occurs is defined as the critical state, corresponding to the final θ_a in Fig. 4a.

Compared to the flowfields at $h_c = 17.78$ mm, the duct with a smaller h_c shows a smaller unstart contraction angle (Fig. 4c). The reason is that with the cowl length and the contraction angle fixed, as the entrance height decreases, the impingement position of the cowl shock moves upstream. As a result, the separation scale relative to the entrance height increases or the mass-averaged Mach number at the throat section decreases, triggering unstart earlier. This trend is more distinctly shown in the unstart boundary distributions in Sec. III.A.

C. Grid Convergence

The numerical method employed in this paper for the unstart phenomenon has been validated for shock-wave/boundary-layer interaction (see Appendix A), and the grid sensitivity of the wall pressure distribution has been investigated [46,50]. To further evaluate the dependence of the computed unstart boundary on grid density, the unstart cowl angle was obtained using three grids for the No. 1 inflow condition. The minimum cell height near the wall is 0.001 mm, and the maximum wall y^+ is 0.8. The region where the shock wave exists ($x = 220 - 400$, $y = 0 - 33$ mm) was refined, and the refinement strategies are as follows: coarse grid (970×305, $dx = 0.186$ mm), medium grid (1400×480, $dx = 0.128$ mm), and dense grid (1900×655, $dx = 0.096$ mm). The cell numbers of the three grids are 600,000, 1,200,000, and 2,200,000, respectively. The numerical results at Mach 3 (Fig. 5 and Table 2) and Mach 6 (Table 3) indicate that the unstart boundary varies slightly with grid density. The maximum deviation relative to the dense grid does not exceed 3%. Therefore, the medium grid was chosen to ensure accuracy while saving computational resources.

III. Generalized Similarity Law for Unstart Boundary

A. Unstart Boundary Represented by Contraction Angle

Similarity analysis [51,52] on the unstart characteristics obtained from CFD simulations was conducted to obtain self-similarity laws and empirical formulas. The unstart contraction angle θ_{un} was obtained under different flow conditions, as shown in Fig. 6. Note that θ_{un} decreases with increasing cowl length L_c and increases with entrance height h_c, Mach number M_∞, and Reynolds number Re_{xc}

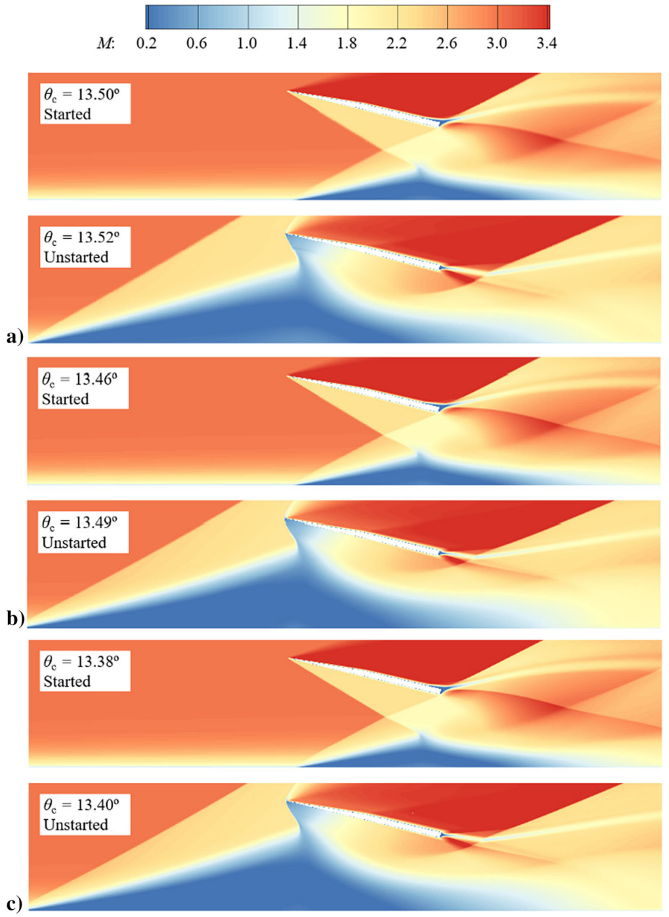

Fig. 5 Critical and unstarted flowfields varying with grid density ($M_\infty = 3$, $L_c = 25.4$ mm, $h = 17.78$ mm): a) coarse grid, b) medium grid, and c) dense grid.

Table 2 Sensitivity of unstart boundary to grid density ($M_\infty = 3$, $L_c = 25.4$ mm, $h = 17.78$ mm)

Parameter	Cell number = 0.6×10^6	Cell number = 1.2×10^6	Cell number = 2.2×10^6
θ_{un}, deg	13.52	13.49	13.40
Error of θ_{un}, deg	0.12	0.09	— —
Error of θ_{un}, %	0.90	0.67	— —

Table 3 Sensitivity of unstart boundary to grid density ($M_\infty = 6$, $L_c = 101.6$ mm, $h = 12.7$ mm).

Parameter	Cell number = 0.6×10^6	Cell number = 1.2×10^6	Cell number = 2.2×10^6
θ_{un}, deg	6.53	6.46	6.35
Error of θ_{un}, deg	0.18	0.11	— —
Error of θ_{un}, %	2.83	1.73	— —

(related to static pressure). The discrete distribution caused by h_c is explained by Fig. 4. For a given h_c, the variation of θ_{un} with L_c depends on the relative length relationship between the cowl and the separation region.

The horizontal axis of Fig. 6 is replaced by the dimensionless cowl length L_c^* [46], as shown in Fig. 7. L_c^* is defined as

$$L_c^* = \frac{L_c}{h_c - \delta_c^*} \tag{4}$$

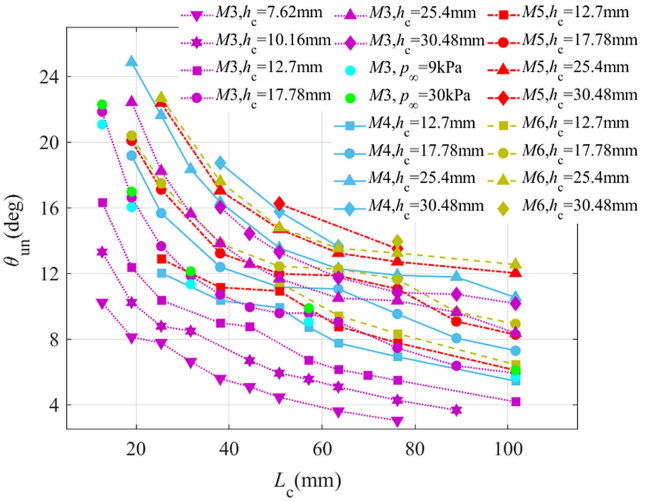

Fig. 6 Unstart boundaries obtained by numerical simulation.

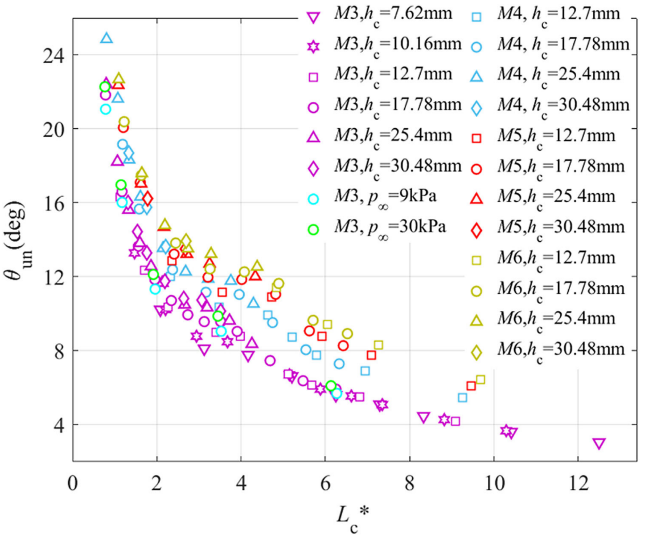

Fig. 7 Unstart boundary correlated with dimensionless cowl length.

In Fig. 7, the data points for different Mach numbers fall onto separated curves, i.e., θ_{un} is a function of (L_c^*, M_∞), exhibiting limited self-similarity. Referring to the similarity theory [51,52], there are two kinds of self-similar solutions. The self-similarity of the first kind can be obtained by dimensional analysis, such as the specific unstart similarity law. The self-similarity of the second kind, taking the form $\Pi/\eta^\alpha = f\ (\xi/\eta^\kappa)$, cannot be fully determined by dimensional analysis. Here Π and ξ are dominant variables, f is a function with the invariable formula, and α and κ are exponents.

In the field of aerodynamics, variables can be corrected by a power form of Mach number, leading to self-similarity. One example is the compressibility correction that establishes a similarity relationship between incompressible and compressible flowfields (Prandtl–Glauert [53] and Karman–Tsien [54,55]). The modified form of the airflow deflection angle (relative to the x-axis) is given by $\theta^* = \theta/(1–M^2)^{1/2}$. Another example is the separation length correlation in hypersonic flow [56].

Considering the positive correlation between the unstart contraction angle and the incoming Mach number, a corrected contraction angle θ_{unM} is proposed:

$$\theta_{unM} = \frac{\theta_{un}}{M_\infty^\alpha} \tag{5}$$

The exponent α that enables data collapse, i.e., $\theta_c/M_\infty^\alpha = f(L_c^*)$, is sought empirically, as with traditional practices. Nowadays the

data-driven neural network can also be used to solve such problems. An optimal solution is

$$\alpha = \begin{cases} 0.4, & 0 < L_c^* < 2.5 \\ 0.5, & 2.5 < L_c^* < 4.3 \\ 0.6, & L_c^* > 4.3 \end{cases} \tag{6}$$

The three values of α correspond to three unstart modes: the short-cowl, transitional, and long-cowl unstart.

The critical flowfields for the three modes are displayed in Fig. 8. For the short-cowl critical state, there is a large separation bubble in the duct, and the separation shock is close to intersecting with the cowl tail. The transitional critical state exhibits a flat separation region with the reflected separation shock impinging on the leeward side of it. The critical separation region is almost independent of the cowl length or throat height for medium L_c^* (θ_{un} decreases from 11.98 to 11.89° as L_c^* increases from 3.2 to 4.0), resulting in the plateaus of θ_{un} in Fig. 7. Hence, the onset of this unstart mode is mainly decided by the inherent self-sustaining mechanism of the flat separation region rather than the relative separation scale, which brings difficulties to theoretical analysis. The long-cowl type shows no obvious separation but has a subsonic region near the throat. Detailed descriptions of the critical states and unsteady processes for the three types can be found in Ref. [46]. The differences in unstart mechanisms (related to the number of shock reflections within the duct) lead to different forms of θ_{unM}, which will be discussed in Sec. IV.

Replacing the longitudinal axis of Fig. 7 by θ_{unM} gives Fig. 9a. The data points of different M_∞ converge onto the same curve, despite the insignificant discrete distribution within $L_c^* = 2.5 \sim 4.3$ causes by the plateaus of θ_{unM}. As discussed in Sec. IV, the plateaus can be correlated with the relative entrance height h_c/δ_c or h_c/δ_c^*. For brevity, the corrected unstart angle θ_{unM} is regarded as a one-variable function of L_c^*, exhibiting self-similarity. The unified fitting formula is

$$\theta_{unM} = \frac{21.9}{L_c^* + 0.8} \tag{7}$$

Overall, the Mach number effect is indirectly reflected through the modified contraction angle θ_{unM}. For different Mach numbers, the distribution of unstart boundaries follows a unified geometric principle. In contrast, the traditional theoretical framework represents the unstart boundary (ICR) as a function of Mach number

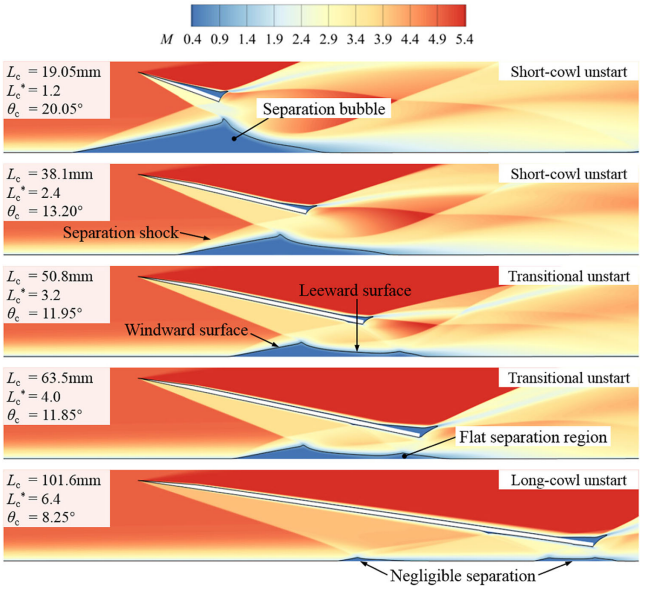

Fig. 8 Critical flowfields of different unstart types ($M_\infty = 5$, $h_c = 17.78$ mm).

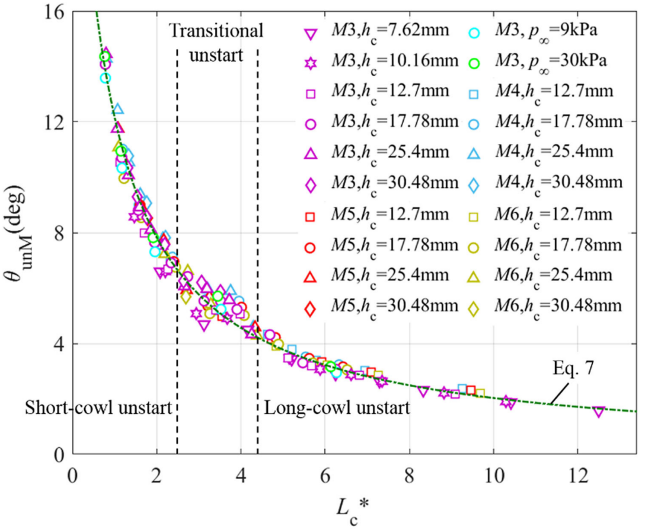

Fig. 9 Extended similarity relationship and fitting formula.

(Fig. 2), breaking the self-similarity based on θ_{unM} and L_c^*. Equations (5–7) provide a new perspective on the unstart phenomenon. Note that the similarity in the unstart phenomenon is limited to the same unstart mode. For example, a duct satisfying the short-cowl unstart condition is similar to another duct that also belongs to the short-cowl unstart rather than the other types.

Since the formulation is based on the two-dimensional frame, three-dimensional effects of SWBLI [57,58] may bring considerable errors for practical inlets unstarting [59,60]. To ensure accuracy, it is suggested that the prediction method in this paper can be used in the rectangular-section inlets with a width-to-height ratio over 3. Despite that the similarity law proposed in this paper cannot cover various practical inlets (e.g., circular-section ducts), it provides a baseline for inlet design, from which the exact unstart characteristics can be obtained with much fewer computing or wind-tunnel resources.

B. Unstart Boundary Represented by Internal Contraction Ratio

The internal contraction ratio (ICR) of a duct is a crucial dimensionless parameter for the unstart phenomenon and is widely used in engineering design. The ICR is defined as the ratio of the cowl lip height to the throat height, and its reciprocal is commonly employed:

$$\mathrm{ICR}^{-1} = \frac{h_t}{h_c} \tag{8}$$

The traditional ICR is an inviscid concept that does not account for the boundary-layer effect and lacks self-similarity. This necessitates the creation of databases for different model scales or Reynolds numbers, consuming significant resources. To address this issue, the previous study [46] has proposed an effective ICR to achieve self-similarity. The effective ICR is defined as the ratio of the inviscid inlet height to the inviscid throat height (subtracting the displacement thickness of the boundary layer). Considering that the displacement thickness at the throat δ_t^* is approximately equal to the value at the entrance δ_c^*, the expression is

$$\mathrm{ICR}_{\text{eff-un}}^{-1} = \frac{h_t - \delta_t^*}{h_c - \delta_c^*} = 1 - L_c^* \sin\theta_{un} \tag{9}$$

However, the self-similarity of effective ICR is irregular for different Mach numbers (Fig. 10).

In this paper, based on θ_{unM}, a corrected ICR is defined to describe the Mach number effect. The expression for the corrected unstart area ratio is

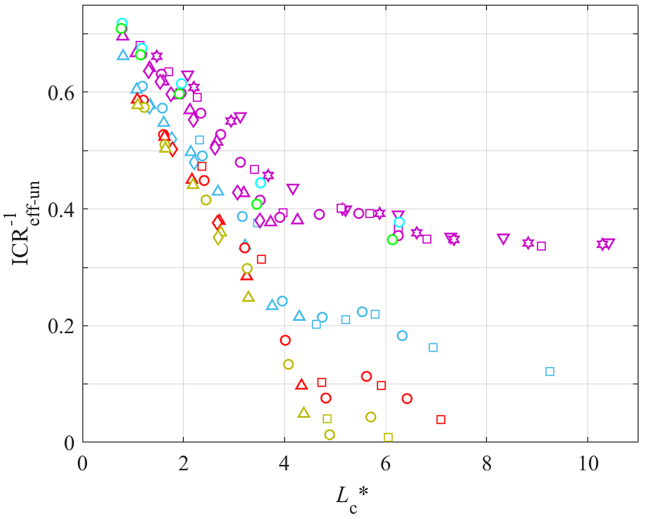

Fig. 10 Effective throat entrance area ratios for unstart at different Mach numbers.

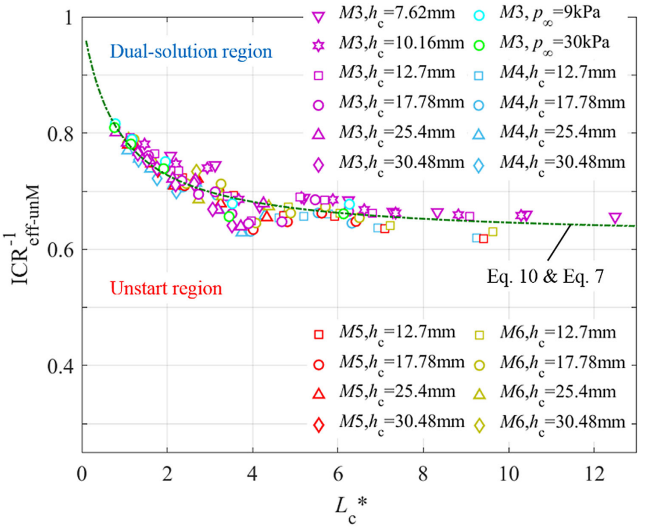

Fig. 11 Extended throat entrance area ratios for unstart.

$$\mathrm{ICR}^{-1}_{\text{eff-unM}} = 1 - L_c^* \sin\left(\frac{\theta_{\text{un}}}{M^\alpha}\right) \tag{10}$$

The unstart boundaries are processed by the modified area ratio (Fig. 11). The data points generally converge to a single curve. The above-curve area represents the dual-solution regime, while the unstart region locates below the curve. The maximum deviation from the empirical formula is about 0.06.

Having achieved a unified description of multivariable effects on the unstart phenomenon, we now present the conversion relationships among the ICR, effective ICR, and corrected ICR for ease of application. Firstly, based on Eq. (9), $\mathrm{ICR}_{\text{eff}}$ can be derived from ICR:

$$\mathrm{ICR}^{-1}_{\text{eff}} = \frac{\mathrm{ICR}^{-1} - \delta_c^*/h_c}{1 - \delta_c^*/h_c} \tag{11}$$

Utilizing that $\sin(\theta_c/M^\alpha) \approx \theta_c/M^\alpha$, $\mathrm{ICR}_{\text{effM}}$ can be calculated from $\mathrm{ICR}_{\text{eff}}$:

$$\begin{aligned}\mathrm{ICR}^{-1}_{\text{effM}} &\approx 1 - \frac{1}{M^\alpha} + \frac{1}{M^\alpha}\left(1 - L_c^*\theta_c\right) \\ &= 1 - \frac{1}{M^\alpha}\left(1 - \mathrm{ICR}^{-1}_{\text{eff}}\right)\end{aligned} \tag{12}$$

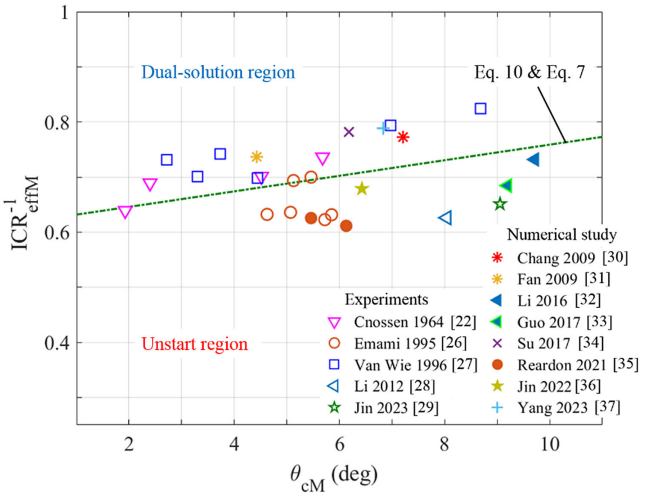

Fig. 12 Empirical formula of unstart boundary represented by θ_{cM} compared to literature data [22,26–37].

If a specific configuration's ICR is required for a given $\mathrm{ICR}_{\text{effM}}$, the conversion process is the reverse of Eqs. (11) and (12):

$$\mathrm{ICR}^{-1}_{\text{eff}} = M^\alpha \mathrm{ICR}^{-1}_{\text{effM}} + 1 - M^\alpha \tag{13}$$

$$\mathrm{ICR}^{-1} = \mathrm{ICR}^{-1}_{\text{eff}}\left(1 - \frac{\delta_c^*}{h_c}\right) + \frac{\delta_c^*}{h_c} \tag{14}$$

Using Eqs. (11) and (12), the unstart boundaries in the literature (see Appendix B) are converted into corrected ICR and presented in Fig. 12. Because of the shoulder or curved surface in practical inlets, it is difficult to accurately define L_c^*, and the contraction angle is more commonly used. Hence, the horizontal axis in Fig. 12 is represented by θ_{cM}, which is equivalent to Fig. 11. Employing Eq. (7) to express L_c^* as the inverse function of θ_{cM} and substituting it into Eq. (10), an empirical formula can be established (the dash-dotted line in Fig. 12). The unstart boundaries obtained by experiments and numerical simulation [22,26–37] generally fall onto the empirical formula, with a maximum deviation within 0.1, which can satisfy the requirement of engineering estimation.

IV. Theoretical Model for Unstart Boundary

The similarity law based on θ_{unM} and L_c^* is essentially an empirical correlation, not directly derived from the first principles of fluid mechanics. Specifically, L_c^* characterizes the relationship between the contracted duct length and the effective capture flow rate or separation scale [46,50], while θ_{unM}, as a key parameter for unifying Mach number effects, the significance of its formula form is unclear. Therefore, simplified theoretical models are established for the three unstart modes to reveal the physical implications of the similarity law.

The similarity of oblique shock angles at the same corrected contraction angle θ_{cM} is examined. The expression for θ_{cM} is consistent with Eq. (2).

$$\theta_c = \theta_{\text{cM}} M_\infty^\alpha \tag{15}$$

For a given θ_{cM} and Mach number, the shock angle β_c is obtained by oblique shock relation:

$$\tan\theta = 2\cot\beta \frac{M^2\sin^2\beta - 1}{M^2(\gamma + \cos 2\beta) + 2} \tag{16}$$

Figure 13 shows the influence of α on cowl shock angle at different Mach numbers. Without correction ($\alpha = 0$), the curves do not intersect. As α increases, the curves begin to intersect (marked by the ellipse), and the θ_{cM} at the intersection point

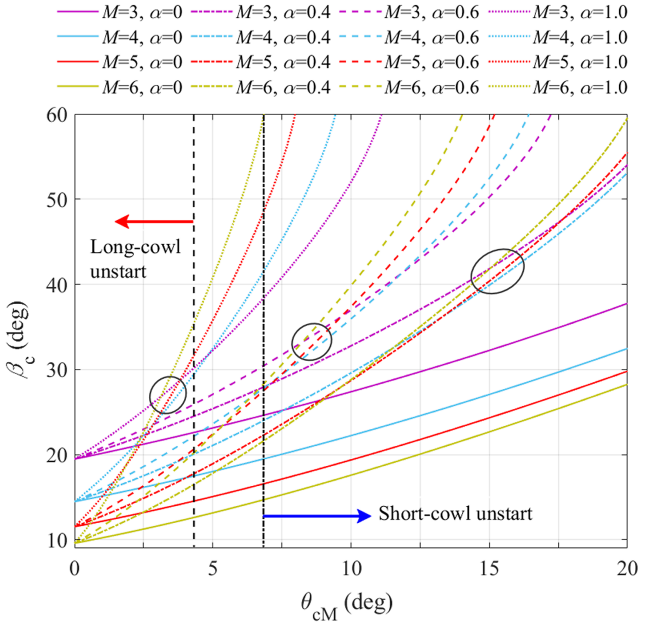

Fig. 13 Relation between cowl shock angle and corrected contraction angle.

gradually decreases. For $\alpha = 0.4$ and 0.6, the dense regions of the curves are (θ_{cM} = 13–18° and 7–10°), respectively, which do not match the ranges of θ_{unM} values for the short-cowl and long-cowl unstart modes in Fig. 8 ($\theta_{cM} > 7.5°$ and $\theta_{cM} < 4.0°$), respectively. Moreover, the intersection is minimal. Therefore, the convergence of cowl shock angles alone is insufficient to explain the similarity of unstart boundaries caused by the correction factor $1/M^{\alpha}$. The SWBLI and shock reflection in the contracted duct must be considered.

A. Short-Cowl Unstart

According to our previous research, the short-cowl unstart is caused by the reflection of the separation shock at the cowl tail. This reflection is affected by three mechanisms (Fig. 14): Firstly, in the started state, as the contraction angle increases, the incidence point of the cowl shock moves forward, and the entire separation region moves upstream. Secondly, since the length of the separation region is positively correlated with the cowl shock strength, at larger contraction angles, the starting position of the separation shock is further upstream, bringing the separation shock closer to the trailing edge of the cowl. In addition, the expansion waves from the cowl tail act on the leeward surface of the separation region, weakening the streamwise pressure difference imposed on the separation region and limiting the separation scale. Based on the above mechanisms, a simplified physical model of the critical state can be established, as shown in Fig. 14.

The critical flow structure of the short-cowl unstart mode is shown in Fig. 14, where $h_{c\text{-inv}}$ represents the inviscid entrance height by subtracting the boundary-layer displacement thickness:

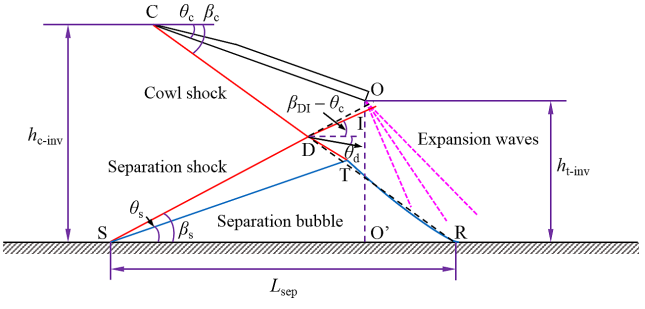

Fig. 14 Schematic critical flow structure of short-cowl unstart.

$$h_{c\text{-inv}} = h_c - \delta_c^* \tag{17}$$

The inviscid throat height of the duct is $h_{t\text{-inv}}$:

$$h_{t\text{-inv}} = h_{c\text{-inv}} - L_c \sin\theta_c \tag{18}$$

The cowl shock and the separation shock intersect at point D, with a vertical coordinate of

$$h_D = L_{sep} \Big/ \left(\frac{1}{\tan\beta_s} + \frac{1}{\tan\beta_c} \right) \tag{19}$$

The separation length L_{sep} is defined as the distance between the separation initiation point S and the reattachment point R. The separation shock angle β_s can be obtained according to the free interaction theory [38]. The expression is

$$\beta_s = \arcsin \sqrt{\frac{1}{M_\infty^2} + C_f \frac{\gamma + 1}{(M_\infty^2 - 1)^{0.25}}} \tag{20a}$$

where C_f is related to the wall friction coefficient. According to Wang's experimental results [61], for $\gamma = 1.4$, Eq. (20a) can be approximated as

$$\beta_s \approx \arcsin \sqrt{\frac{1}{M_\infty^2} + \frac{1}{5.8(M_\infty^2 - 1)^{0.25}}} \tag{20b}$$

In Fig. 15, the predicted results of Eq. (20b) agree well with CFD results, and the influence of Reynolds number on the separation shock angle is not significant.

The projected height of the deflected separation shock at the throat position is denoted by $h_{IO'}$. When unstart is triggered, shock DI reflects at point O at the cowl trail, so $h_{IO'}/h_{t\text{-inv}} \geq 1$ is taken as the unstart trigger. Conversely, in the started state, $h_{IO'}/h_{t\text{-inv}} < 1$.

$$h_{IO'} = h_D + \left(L_{SO'} - h_D/\tan\beta_s\right) \tan\left(\beta_{DI} - \theta_c\right) \tag{21}$$

Here, $L_{SO'}$ is the distance from the leading edge of the separation bubble to the throat,

$$L_{SO'} = L_{sep} + L_c \cos\theta_c - h_{c\text{-inv}}/\tan\beta_c \tag{22}$$

and θ_d is the angle between the downstream flow direction and the x-axis at point D, which can be approximated by

$$\theta_d \approx \theta_c - \theta_s \tag{23}$$

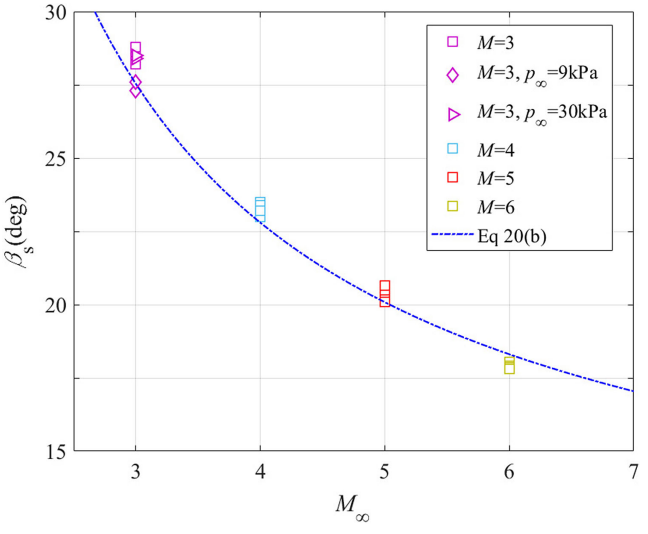

Fig. 15 Separation shock angle varying with Mach number.

The separation angle θ_s is obtained by substituting M_∞ and β_s into Eq. (16). The flow deflection angle of shock DI is

$$\theta_{\mathrm{DI}} = \theta_c - \theta_d \approx \theta_s \tag{24}$$

The shock angle β_{DI} is obtained by substituting the Mach number M_c behind the cowl shock and θ_{DI} into Eq. (16). The expression of M_c is

$$M_c^2 = \frac{M_\infty^2 + \frac{2}{\gamma-1}}{\frac{2\gamma}{\gamma-1}(M_\infty \sin\beta_c)^2 - 1} + \frac{(M_\infty \cos\beta_c)^2}{\frac{\gamma-1}{2}(M_\infty \sin\beta_c)^2 + 1} \tag{25}$$

The estimation of separation scale is crucial to the model accuracy. For simplicity, it is assumed that the reattachment point of the separation bubble coincides with the impingement point of the cowl shock. According to numerical results, this assumption is generally valid for critical flowfields with strong tail expansion waves. The distance between the impingement point of the cowl shock and the separation point is the separation length L_{sep}. Existing research on separation length in turbulent flow is still insufficient. Zhao [62] proposed a self-similar formula for turbulent SWBLI based on Katzer's laminar SWBLI study [63].

$$L_{\mathrm{sep0}} = A\delta_c \sqrt{Re_{xc}} M^{-0.5} \tag{26}$$

where A is a function of contraction angle:

$$A = 1.2\left(\theta_c - \frac{\pi}{180}\left[4.2\ \lg\left(Re_{xc}\right) - 27.5\right]\right)^4 \tag{27}$$

However, Eqs. (26) and (27) do not reflect the effect of the tail expansion waves (see Appendix C). According to Grossman [64,65] and Fan [66], the expansion waves reduce the separation length. Since the expansion wave angle, impingement position, and pressure ratio are coupled with Mach number, throat height, and contraction angle, it is hard to give the streamwise pressure difference of the separation region in a simple formula and thus determine the separation scale. In this paper, Eqs. (26) and (27) are modified to obtain the distribution law of separation length under the expansion wave effect.

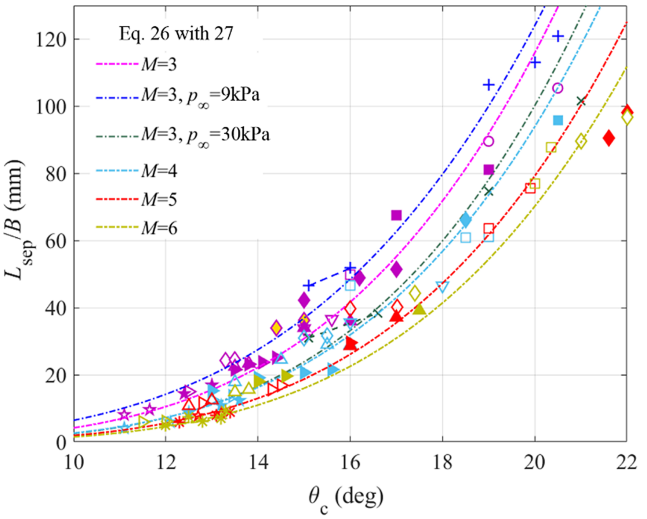

Fig. 16 Corrected relation between separation length and contraction angle (legend of data points is the same as Fig. A1: magenta—$M_\infty = 3$, $p_\infty = 18.77$ kPa; blue—$M_\infty = 3$, $p_\infty = 9$ kPa; green—$M_\infty = 3$, $p_\infty = 30$ kPa; light blue—$M_\infty = 4$; red—$M_\infty = 5$; yellow green—$M_\infty = 6$).

$$B = \begin{cases} 0.0435\dfrac{L_c^2}{\delta_c^* h_{c\text{-inv}}}, & L_c^* < 2.5 \\ 1, & L_c^* > 2.5 \end{cases} \tag{29}$$

Processing the data in Appendix C with Eqs. (28) and (29) gives Fig. 16. The vertical axis is the ratio of the separation length L_{sep} to the correction factor B (i.e., L_{sep0}), which leads to a self-similar formula. The curves in Fig. 16 are obtained by Eqs. (26) and (27). For each incoming flow condition, the data points converge onto the corresponding curve, roughly satisfying self-similarity. However, the curve values are higher than CFD data when $\theta_c > 20°$, which needs to be improved in future research.

From Eqs. (18), (19), (21), and (22), the ratio of the projected height of the separation shock to the throat height can be obtained:

$$\begin{aligned} \frac{h_{\mathrm{IO'}}}{h_{t\text{-inv}}} &= \frac{h_D + (L_{\mathrm{SO'}} - h_D/\tan\beta_s)\tan(\beta_{\mathrm{DI}} - \theta_c)}{h_{c\text{-inv}} - L_c \sin\theta_c} \\ &= \frac{L_{\mathrm{sep}}\left[\tan\beta_c + \tan(\beta_{\mathrm{DI}} - \theta_c)\right] \Big/ \left(1 + \frac{\tan\beta_c}{\tan\beta_s}\right) + \left(L_c\cos\theta_c - \frac{h_{c\text{-inv}}}{\tan\beta_c}\right)\tan(\beta_{\mathrm{DI}} - \theta_c)}{h_{c\text{-inv}} - L_c \sin\theta_c} \end{aligned} \tag{30a}$$

Both the right-hand-side numerator and denominator are divided by $h_{c\text{-inv}}$. For the short-cowl cases ($L_c^* < 2.5$), substituting Eqs. (4), (28), and (29) gives

$$\frac{h_{\mathrm{IO'}}}{h_{t\text{-inv}}} = \frac{0.0435 L_c^* \frac{L_{\mathrm{sep0}}}{\delta_c^*}\left[\tan\beta_c + \tan(\beta_{\mathrm{DI}} - \theta_c)\right] \Big/ \left(1 + \frac{\tan\beta_c}{\tan\beta_s}\right) + \left(L_c^*\cos\theta_c - \frac{1}{\tan\beta_c}\right)\tan(\beta_{\mathrm{DI}} - \theta_c)}{1 - L_c^* \sin\theta_c} \tag{30b}$$

The separation lengths in the started state varying with the contraction angle, entrance height, wedge length, Mach number, and Reynolds number are given in Appendix C. Since the separation length is affected by the cowl length more significantly than the entrance height, L_c^* is chosen to represent the relation between the cowl length and the entrance height, and then a correction factor B can be derived by multiplying L_c^* and the cowl length scaled by displacement boundary-layer thickness $L_c/\delta c^*$. In this way, the separation length is estimated by Eqs. (28) and (29).

$$L_{\mathrm{sep}} = AB\delta_c \sqrt{Re_{xc}} M^{-0.5} \tag{28}$$

The variation of $h_{\mathrm{IO'}}/h_{t\text{-inv}}$ with θ_{cM} can be derived by substituting Eqs. (15), (16), (20b), and (23–27) into Eq. (30b), as shown in Fig. 17. It is worth noting that if the separation point is downstream of the throat ($L_{\mathrm{SO'}} < 0$), $h_{\mathrm{IO'}}/h_{t\text{-inv}}$ will reach negative values. Thus, $h_{\mathrm{IO'}}/h_{t\text{-inv}}$ is presumed to be zero for simplicity. In Fig. 17, for a fixed θ_{cM}, $h_{\mathrm{IO}}/h_{t\text{-inv}}$ increases with L_c^*, causing a leftward shift of the curve. The curves of the same L_c^* cluster, particularly within $L_c^* = 0.6$–1.5. The abscissa of the intersection point between the curve and the horizontal line $h_{\mathrm{IO'}}/h_{t\text{-inv}} = 1$ corresponds to the unstart contraction angle θ_{unM}. The scatter of θ_{unM} under different flow conditions is small (0.2–0.8°), indicating that θ_{unM} is approximately a function of L_c^* only.

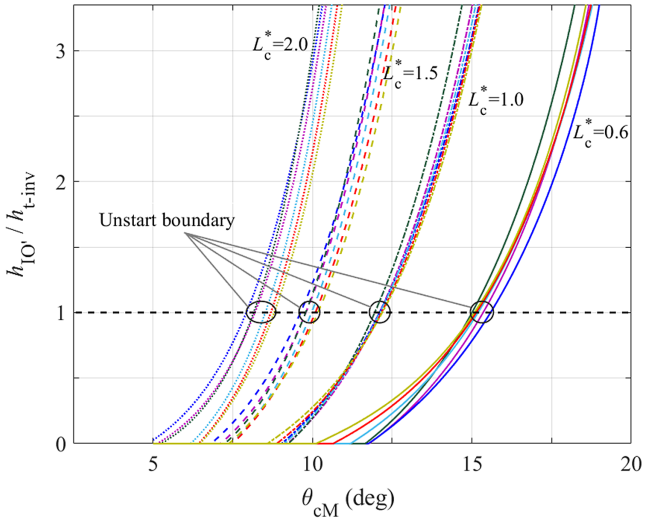

Fig. 17 The ratio of the projected height of the separation shock to the throat height varying with corrected contraction angle.

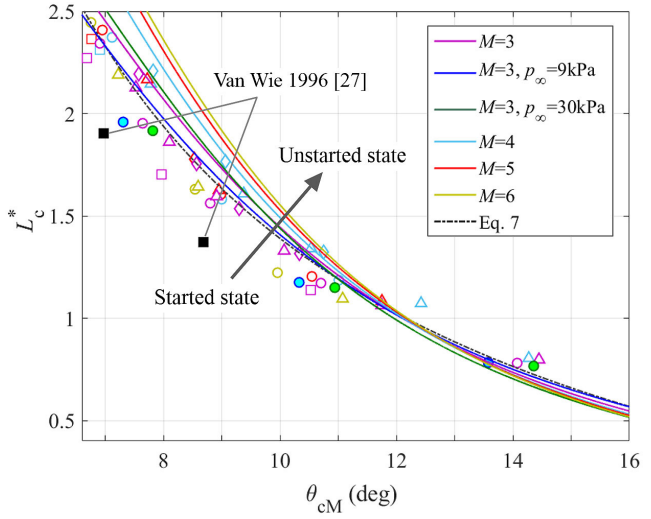

Fig. 18 Short-cowl unstart boundaries predicted by theoretical model compared to empirical formula, CFD data points, and experimental data [27].

The process of seeking the intersection points in Fig. 17 is as follows: for different θ_{cM} values, determine the corresponding L_c^* such that the left side of Eq. (30b) equals 1. Numerical methods (e.g., the bisection method) can be used to solve the equation. The unstart boundaries for various flow conditions are represented as $L_c^* - \theta_{cM}$ curves (Fig. 18). The horizontal and vertical axes in Fig. 18 are swapped based on Fig. 8. If a parameter point enters the region above the curve from the lower region, unstart occurs. The curves converge near the empirical formula (7). Compared to CFD results, the maximum deviation measured by θ_{cM} is about 1.1° with a relative error of 15%, which satisfies engineering estimation requirements. However, the deviation relative to Van Wie's experimental results [27] is 16–18%, which may be caused by the three-dimensional effects in the wind tunnel. For smaller θ_{cM}, the theoretical model gives optimistic predictions, and the self-similarity is broken. The reason is that the critical flow regime deviates from the hypothesis in Fig. 14 near the unstart mode transition point.

In Figs. 13 and 16, the shock angle and separation scale are not self-similar with the Mach number separately; however, the theoretical model combining these two components exhibits self-similarity. Therefore, the self-similarity of θ_{unM} originates from the coupling between the cowl shock angle and the geometric characteristics of the separation region.

B. Transitional Unstart

Compared to the short-cowl unstart, the transitional unstart is accompanied by shock reflection within the duct, besides the oblique-shock-induced separation. For simplicity, an idealized model for shock reflections is first presented, as shown in Fig. 19. The shock initiation points (reflection points) are numbered 1–4, with the lengths of the shock segments denoted as L_1–L_3, and the distances between the shock initiation points denoted as L_{13} and L_{24}. The total number of shock initiation points within the contraction duct is n_t. According to CFD results and unstart mode theory, n_t equals 3 for the transitional unstart.

More generally, indexing the reflection points by i, the shock length L_i and the distance between two adjacent shock reflection points $L_{i,i+2}$ can be expressed as follows:

$$L_i = \begin{cases} \dfrac{h_{c\text{-inv}}}{\sin\beta_1}, & i = 1 \\ h_{c\text{-inv}} \dfrac{\sin(\beta_1 - \theta_c)}{\sin\beta_1} \cdots \dfrac{\sin(\beta_{i-1} - \theta_c)}{\sin\beta_{i-1}} \dfrac{1}{\sin\beta_i}, & i > 1 \end{cases} \tag{31}$$

$$L_{i,i+2} = L_i \cos(\beta_i - \theta_c) + L_{i+1} \cos\beta_{i+1} \tag{32}$$

Using oblique shock relations, one can obtain the shock angle β_i and subsequently obtain the Mach number behind the shock M_i:

$$\tan\theta_c = 2\cot\beta_i \frac{M_{i-1}^2 \sin^2\beta_i - 1}{M_{i-1}^2(\gamma + \cos 2\beta_i) + 2} \tag{33}$$

$$M_i^2 = \frac{M_{i-1}^2 + \frac{2}{\gamma-1}}{\frac{2\gamma}{\gamma-1}(M_{i-1}\sin\beta_i)^2 - 1} + \frac{(M_{i-1}\cos\beta_i)^2}{\frac{\gamma-1}{2}(M_{i-1}\sin\beta_i)^2 + 1} \tag{34}$$

M_{i-1} is replaced by M_∞ when $i = 1$.

The triggering of the transitional unstart is related to L_{24}. As θ_c increases, the shock angles β_1, β_2, and β_3 all increase, making L_{24} decrease. Due to the small separation bubble upstream of reflection point 2 and the adverse pressure gradient imposed by shock L_3 on the downstream boundary layer, a continuous separation region forms between points 2 and 4 for relatively large θ_c. Existing literature has noted that, as the spacing between shock reflection points decreases, two small separation bubbles merge with a sudden increase in separation size [67–69]. It can be inferred that as L_{24} further decreases, the high pressure at point 4 propagates through the subsonic region to point 2, which drives the separation region to grow and then triggers unstart. Therefore, L_{24} scaled by L_{sep} (the separation length induced solely by the cowl shock) can be regarded as the governing variable for the transitional unstart. Assuming that unstart occurs when $L_{24}/L_{sep} \le k$ (k is an empirical value), the simplified model in Fig. 19 can be modified to account for the separation bubble, as shown in Fig. 20.

In Fig. 20, because the separation bubble is small, the deflection of the separation shock at the intersection point can be ignored, and the shock angle $\beta_{2'}$ is approximately equal to β_2. The shock lengths L_{2m} and L_{3m} are increased compared to those in Fig. 19, and the expressions are

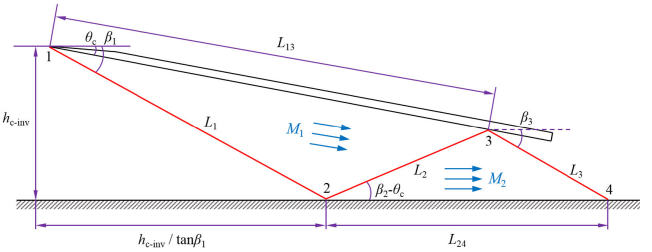

Fig. 19 Shock reflection regime in contraction duct.

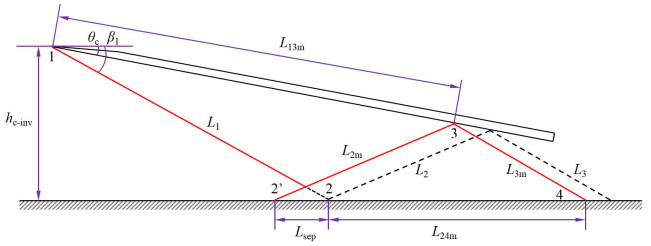

Fig. 20 Schematic shock reflection structure with separation bubble.

$$L_{2m} = L_2 + L_{\text{sep}} \frac{\sin\theta_c}{\sin\beta_2} \tag{35}$$

$$L_{3m} = L_3 + L_{\text{sep}} \frac{\sin\theta_c}{\sin\beta_2} \frac{\sin(\beta_2 - \theta_c)}{\sin\beta_3} \tag{36}$$

The modified distances between shock reflection points are

$$L_{13m} = L_1 \cos(\beta_1 - \theta_c) + L_{2m} \cos\beta_2 - L_{\text{sep}} \cos\theta_c \tag{37}$$

$$L_{24m} = L_{2m} \cos(\beta_2 - \theta_c) + L_{3m} \cos\beta_3 - L_{\text{sep}} \tag{38}$$

Figures 8 and 11 indicate that the data points of the transitional unstart are discrete to some extent and not strictly self-similar. There are two reasons. Firstly, with the fixed number of shock initiation points, n_t, of 3, L_{24m}/L_{sep} does not vary with L_c within a certain range. Hence, a single θ_{unM} may correspond to several L_c^* in the critical state. The cowl length range for $n_t = 3$ is

$$\frac{L_{13m}}{h_{c\text{-inv}}} < L_c^* < \left(\frac{h_{c\text{-inv}}}{\sin\beta_1} + L_{24m}\right) \Big/ (h_{c\text{-inv}} \cos\theta_c) \tag{39}$$

The right-hand side corresponds to the situation where the wedge tail and point 4 share the same x-coordinate.

Secondly, θ_{unM} is inherently not self-similar for the transitional unstart. L_{24} is related to $h_{c\text{-inv}}$, and L_{sep} depends on incoming flow condition and shock strength. Thus, L_{24m}/L_{sep} is not reducible to a univariate function like $h_{ss}/h_{t\text{-inv}}$. The expression of L_{24m}/L_{sep} is

$$\begin{aligned}\frac{L_{24m}}{L_{\text{sep}}} &= \frac{L_2 \cos(\beta_2 - \theta_c) + L_3 \cos\beta_3}{A\delta_c \sqrt{Re_{xc}} M_\infty^{-0.5}} \\ &\quad + \frac{\sin\theta_c}{\sin\beta_2}\left[\cos(\beta_2 - \theta_c) + \frac{\sin(\beta_2 - \theta_c)}{\tan\beta_3}\right] - 1 \\ &= \frac{h_{c\text{-inv}}}{\delta_c} f_3(\theta_c, M_\infty, Re_{xc}) + f_4(\theta_c, M_\infty) - 1\end{aligned} \tag{40}$$

Here, L_2 and L_3 are both proportional to $h_{c\text{-inv}}$. The first term on the right side of Eq. (40) can be transformed into the product of $h_{c\text{-inv}}/\delta_c$ and function f_3.

Figure 21 shows the variation of L_{24m}/L_{sep} with θ_{cM} for different incoming flow conditions. For each case, $h_{c\text{-inv}}/\delta_c$ takes on values of 1, 3.5, and 6. For $M_\infty = 3$, despite $h_{c\text{-inv}}/\delta_c$ is fixed, the curves scatter under different Reynolds numbers Re_{xc} (see function f_3 in Eq. (40)). The scattering of curves for different M_∞ can also be explained by Eq. (40). Taking the empirical value $k = 5$ as the unstart trigger, the abscissa of the intersection point between the curves and the horizontal line $L_{24m}/L_{\text{sep}} = 5$ corresponds to θ_{unM}. In Fig. 21, θ_{unM} increases with Re_{xc} and $h_{c\text{-inv}}/\delta_c$ and decreases with M_∞.

To determine the relationship between θ_{unM} and L_c^*, the left side of Eq. (40) is set to 5, and the equation is solved using numerical methods. For a given incoming flow condition, the θ_{cM} that satisfies the requirements is sought in the range of $h_{c\text{-inv}}/\delta_c = 1.0$–$6.5$ (which is close to the parameter range used in the numerical simulations of this paper), and the corresponding L_c^* range is given by Eq. (39). In this way, two $\theta_{\text{cM}} - L_c^*$ curves are obtained for each

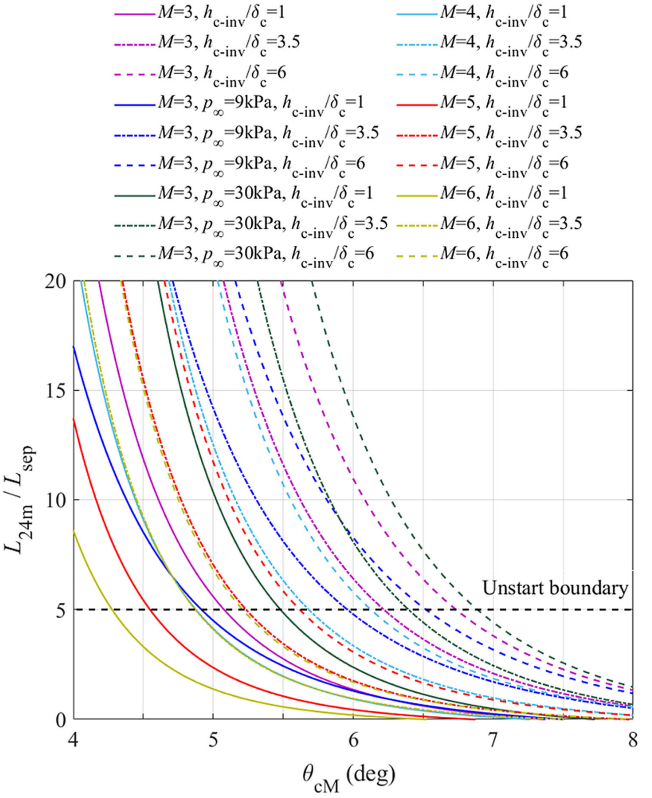

Fig. 21 Scaled distance between reflection points L_{24m}/L_{sep} as functions of corrected contraction angle θ_{cM}.

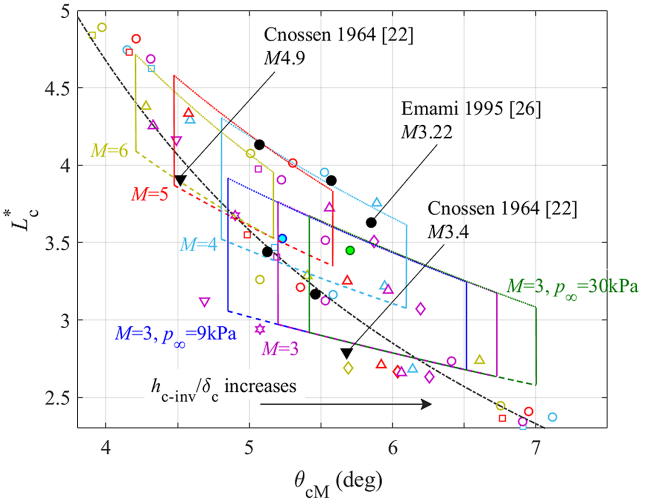

Fig. 22 Transitional unstart boundary predicted by theoretical model ($h_{c\text{-inv}}/\delta_c = 1.0$–$6.5$) compared to empirical equation, CFD data, and experimental data [22,26].

flow condition (Fig. 22). The six quadrilateral regions in Fig. 22 are unstart regions. If the parameter point enters the regions from below or left, an unstart occurs.

For $2.5 < L_c^* < 4.3$, most data points are located within the corresponding unstart region, and only a few data points deviate from both the quadrilateral regions and the empirical formula. As M_∞ increases, the unstart region moves toward the upper left and narrows. As Re_{xc} increases, the upper and lower boundaries of the transitional unstart region remain unchanged, while the left and right boundaries move to the right simultaneously. In summary, for $2.5 < L_c^* < 4.3$, a higher M_∞ allows a larger L_c^* and a smaller θ_{cM} in the stated state, while a higher Re_{xc} allows a smaller L_c^* and a larger θ_{cM}.

Compared to experimental results [22,26], the model can capture a part of transitional unstart boundaries; hence, it can meet the accuracy requirements of rapid estimation. A refined model would need to explain the physical significance of the critical shock reflection point spacing and provide a more reasonable value of k (it possibly depends on M_∞ and Re_{xc}), which awaits further research on the separation caused by two incident shocks [70–72].

C. Long-Cowl Unstart

Based on the classical isentropic theory, the mechanism of long-cowl unstart can be proposed considering the total pressure loss and flow parameter discontinuities caused by the shock waves. The multiple reflections of the shock wave in the contraction duct decelerate the airflow and reduce the mass-averaged Mach number at the throat position M_t. Flow choke will occur when M_t is too low. In this paper, $M_t = 1$ is assumed to be the trigger of unstart.

For long-cowl cases, the contraction angle is generally small ($\theta_{\mathrm{unM}} < 4°$), and the shock-induced separation can be ignored. Based on the number of shock initiation (reflection) points n_t in the flow path, a series of simplified regimes can be obtained, as shown in Fig. 23. For simplicity, the streamwise boundary-layer thickening caused by shock reflections is not considered. When the cowl is very long, the terminal shock approaches a normal shock, and the boundary layer near the throat thickens significantly, with M_t approaching 1. Therefore, this paper assumes that unstart will occur directly when $n_t > 6$. The following analysis only includes the cases of $n_t = 1$–6.

The throat Mach number is related to n_t, which needs to be determined first. For a given flow condition (M_∞, Re_{xc}, or δ_c^*) and configuration (h_c, θ_c), the following geometric relationship can be derived:

$$n_t = \begin{cases} 1, & 0 < L_c^* < 1/(\tan\beta_1 \cos\theta_c) \\ 2, & 1/(\tan\beta_1 \cos\theta_c) < L_c^* < \dfrac{L_{13}}{h_{c\text{-inv}}} \\ 3, & \dfrac{L_{13}}{h_{c\text{-inv}}} < L_c^* < \left(\dfrac{h_{c\text{-inv}}}{\sin\beta_1} + L_{24}\right) \Big/ (h_{c\text{-inv}} \cos\theta_c) \\ 4, & \left(\dfrac{h_{c\text{-inv}}}{\sin\beta_1} + L_{24}\right) \Big/ (h_{c\text{-inv}} \cos\theta_c) < L_c^* < \dfrac{L_{13} + L_{35}}{h_{c\text{-inv}}} \\ 5, & \dfrac{L_{13} + L_{35}}{h_{c\text{-inv}}} < L_c^* < \left(\dfrac{h_{c\text{-inv}}}{\sin\beta_1} + L_{24} + L_{46}\right) \Big/ (h_{c\text{-inv}} \cos\theta_c) \\ 6, & L_c^* > \left(\dfrac{h_{c\text{-inv}}}{\sin\beta_1} + L_{24} + L_{46}\right) \Big/ (h_{c\text{-inv}} \cos\theta_c) \end{cases} \tag{41}$$

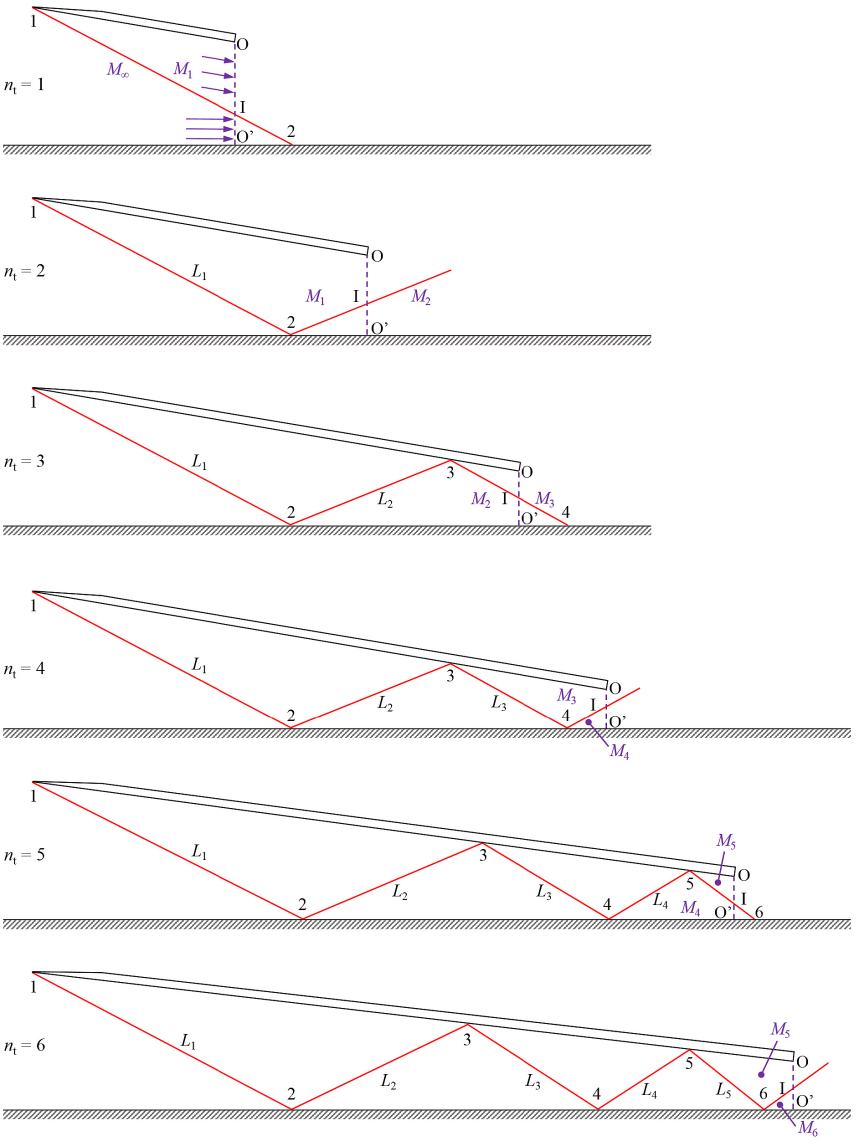

Fig. 23 Flow structure of shock wave reflections in contraction duct ($n_t = 1 - 6$).

In Eq. (41), the variables are obtained from Eqs. (31–34). According to Eqs. (31) and (32), $L_{i,i+2}$ is directly proportional to $h_{c\text{-inv}}$, and hence $h_{c\text{-inv}}$ is actually eliminated.

The formula of M_t depends on the parity of n_t. In Fig. 23, when n_t is odd, the terminal shock reflection point upstream of the throat is located on the upper wall, while when n_t is even, it is located on the lower wall. The projected height of the last shock wave at the throat is denoted by $h_{\mathrm{IO}'}$:

$$h_{\mathrm{IO}'} = \begin{cases} (h_c/\tan\beta_1 + L_{24} + \cdots + L_{n_t-1,n_t+1} - L_c\cos\theta_c)\tan\beta_{n_t}, & n_t = 1,3,5\ldots \\ [L_c\cos\theta_c - (h_c/\tan\beta_1 + L_{24} + \cdots + L_{n_t-2,n_t})]\tan(\beta_{n_t} - \theta_c), & n_t = 2,4,6\ldots \end{cases} \tag{42}$$

In Eq. (42), if $n_t = 1$ or 2, the terms about reflection points spacing $L_{24}\ldots L_{i,i+2}$ are redundant. The mass-averaged Mach number at the throat is

$$M_t = \begin{cases} \dfrac{M_{n_t-1}\rho_{n_t-1}U_{n_t-1}h_{\mathrm{IO}'} + M_{n_t}\rho_{n_t}U_{n_t}(h_t - h_{\mathrm{IO}'})\cos\theta_c}{\rho_\infty U_\infty h_c}, & n_t = 1,3,5\ldots \\ \dfrac{M_{n_t-1}\rho_{n_t-1}U_{n_t-1}(h_t - h_{\mathrm{IO}'})\cos\theta_c + M_{n_t}\rho_{n_t}U_{n_t}h_{\mathrm{IO}'}}{\rho_\infty U_\infty h_c}, & n_t = 2,4,6\ldots \end{cases} \tag{43}$$

Here, the flow velocity U_i is

$$U_i = M_i\sqrt{\gamma\frac{p_i}{\rho_i}} \tag{44}$$

The density ρ_i and static pressure p_i behind the shock are determined by oblique shock relation:

$$\frac{\rho_i}{\rho_{i-1}} = \frac{(\gamma+1)(M_{i-1}\sin\beta_i)^2}{2+(\gamma-1)(M_{i-1}\sin\beta_i)^2} \tag{45a}$$

$$\frac{\rho_i}{\rho_\infty} = \frac{\rho_i}{\rho_{i-1}}\cdots\frac{\rho_1}{\rho_\infty} \tag{45b}$$

$$\frac{p_i}{p_{i-1}} = 1 + \frac{2\gamma}{\gamma+1}[(M_{i-1}\sin\beta_i)^2 - 1] \tag{46a}$$

$$\frac{p_i}{p_\infty} = \frac{p_i}{p_{i-1}}\cdots\frac{p_1}{p_\infty} \tag{46b}$$

For different L_c^*, the variation of M_t with θ_{cM} is calculated by Eqs. (31–34) and (41–46), as displayed in Fig. 24. With L_c^* fixed, as θ_{cM} increases, the curves of different M_∞ first converge and then diverge, and the curves roughly intersect at $M_t = 1$, which is the unstart boundary. Figure 24 indicates that although the θ_{cM} correction fails to achieve similarity in the first shock angle (Fig. 13), the throat Mach number M_t after multiple shock reflections exhibits self-similarity within a specific θ_{cM} range. The abscissa of the intersection point between the curves and the $M_t = 1$ horizontal line is θ_{unM}, of which the scatter range is about 0.1–0.3°. As L_c^* increases, θ_{unM} decreases, consistent with the data trend in Fig. 9.

Setting the left side of Eq. (43) equal to 1, for different θ_{cM}, the solution represented by L_c^* is sought (Fig. 25). The curves converge near the empirical Eq. (7), but as L_c^* becomes very large, the theoretical curves fall below Eq. (7) and exhibit a divergent trend. For $L_c^* < 15$, compared to Eq. (7) and CFD data, the maximum deviation of θ_{unM} is 0.21 and 0.35°, which corresponds to errors of 0.62 and 1.02° in θ_{un}, respectively. The reason for this deviation may be that when the cowl is very long, the streamwise development of the boundary layers on the upper and lower walls becomes significant [39]. The boundary-layer development dominates the Mach number distribution at the throat and the trigger of unstart, while the effect of shock reflection is secondary. This allows a larger θ_{unM} for a fixed L_c^*. Because such long inlet ducts are seldom used in engineering, the theoretical model can be simply modified to further approach the empirical formula. Assuming that $M_t = 0.6$ when unstart occurs, the theoretical curves of small θ_{cM} are raised (dashed line in Fig. 25), reducing the deviation of θ_{unM} to 0.15 and 0.27° compared to Eq. (7) and CFD data, respectively. Generally, the present model agrees well with the experimental data [22,27].

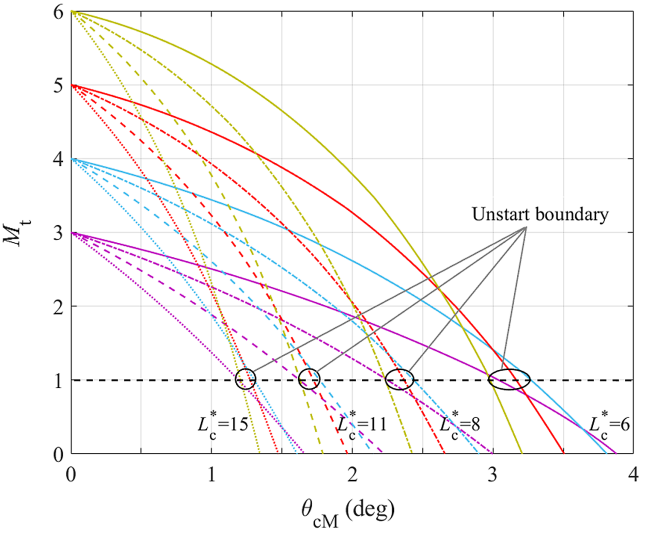

Fig. 24 Mass-averaged throat Mach number as functions of corrected contraction angle.

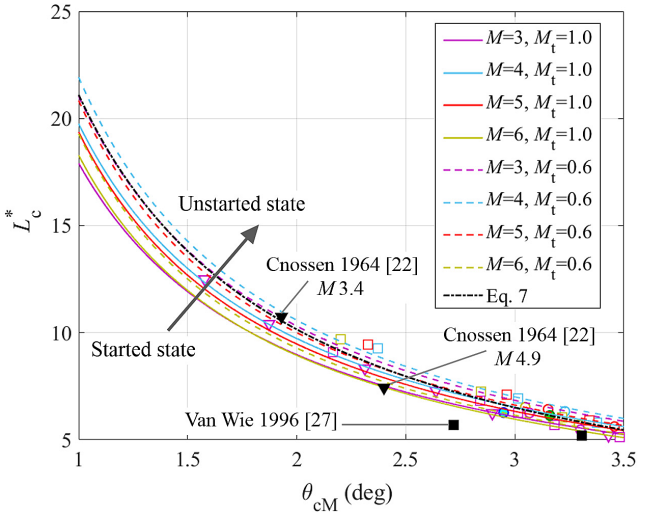

Fig. 25 Long-cowl unstart boundary predicted by theoretical model compared to empirical formula, CFD data points, and experimental data [22,27].

V. Extended Similarity Law for Critical Pressure Rise

Existing studies have pointed out that, for different unstart modes, the growth of the separation region is essentially driven by the streamwise pressure difference [46,50]. Wall pressure is an important parameter in SWBLI and a primary criterion for the operating state of actual hypersonic inlets [21,45,73,74]. Therefore, this paper analyzes the wall pressure characteristics under various conditions and explores their similarity law. Similar to Sec. IV, this section focuses on the critical conditions.

Figure 26a shows the wall pressure curves in critical state for various configurations at $M_\infty = 5$. The initial pressure rise of each curve corresponds to the separation point, and the wall pressure peak $p_{\max}$ occurs near the throat, with the wall pressure rapidly decreasing downstream of the pressure peak. For the same entrance height h_c, as the cowl length L_c increases, the separation point moves downstream, and $p_{\max}$ increases. Keeping L_c constant, as h_c increases, the separation point moves upstream, and $p_{\max}$ changes slightly. Therefore, the pressure rise characteristic of the separation region is related to L_c^*. According to existing research, the relative streamwise pressure difference, $p_{\max}/p_\infty - 1$, is used to approximately characterize the separation scale. The $p_{\max}/p_\infty - 1$ for different Mach numbers are shown as functions of L_c^* in Fig. 26b. The critical pressure difference increases with Mach number and L_c^*, and the curves are discretely distributed.

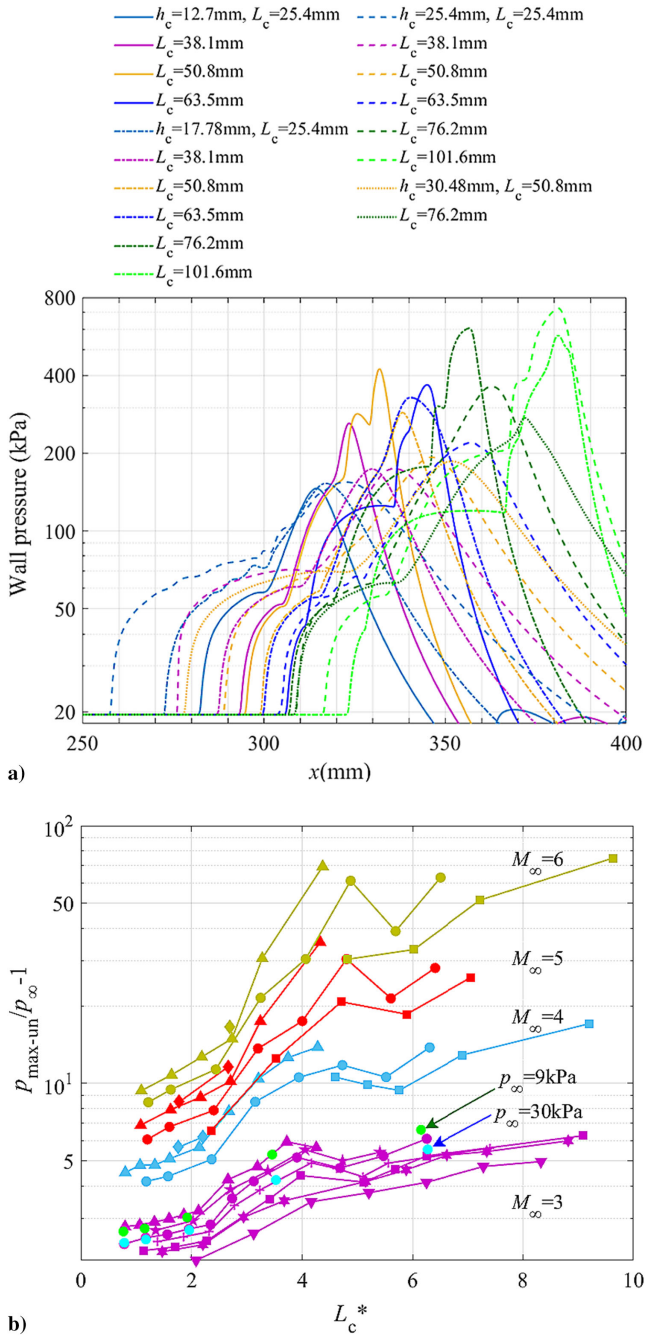

Fig. 26 Wall pressure characteristics in unstart critical state: a) wall pressure curves varying with contraction angle and entrance height ($M_\infty = 5$); b) dimensionless pressure peaks under different conditions.

Based on the correlation between the streamwise pressure difference and the characteristic separation scale [75–77], the self-similar pressure rise p^*_{unc} has been proposed in our previous study [46,50] by correlating the separation scale with the entrance height:

$$p^*_{\text{unc}} = \left(\frac{p_{\max\text{-un}}}{p_\infty} - 1\right)^b \frac{\delta_c^*}{h_c} \propto \frac{L_{\text{sep-un}}}{h_c} \tag{47}$$

$L_{\text{sep-un}}$ is the critical characteristic separation length. For Mach 3, $b = 3$. For other Mach numbers in this paper, b can be obtained by data fitting.

$$b = 1.8 + 1.2 \times 0.5^{M_\infty - 3} \tag{48}$$

The data in Fig. 26b are processed by Eqs. (47) and (48) and shown in Fig. 27a. The curves converge for the same M_∞, but still scatter for different M_∞.

To develop a wall pressure criterion for variable Mach numbers, a simple assumption is made that the separation scale at a given contraction angle is mainly decided by the cowl shock strength [78]. Therefore, the cowl-shock pressure rise p_1/p_∞ can be incorporated into p^*_{unc}, and a new similarity variable p^*_{uncM} can be constructed:

$$p^*_{\text{uncM}} = f\left(\frac{p_{\max\text{-un}}}{p_\infty}, \frac{\delta_c^*}{h_c}, \frac{p_1}{p_\infty}\right) \tag{49}$$

A trial power function of $p_1/p_\infty - 1$ is chosen to further modify p^*_{unc}.

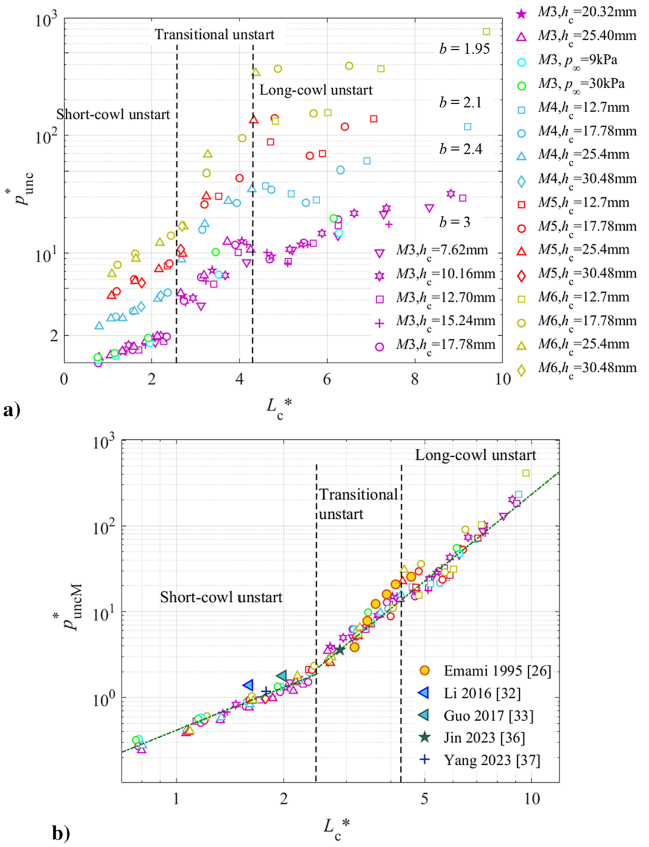

Fig. 27 Self-similar wall pressure characteristics in critical state: a) specific similarity law for different Mach numbers; b) extended similarity law compared to literature data [26,32,33,36,37].

$$p^*_{\text{uncM}} = \frac{\delta^*_c}{h_c}\frac{(p_{\text{max-un}}/p_\infty - 1)^b}{(p_1/p_\infty - 1)^d} \tag{50}$$

in which p_1/p_∞ is obtained by θ_c and M_∞ Eq. (46a). The exponent d depends on unstart mode:

$$d = \begin{cases} 1.2, & 0 < L^*_c < 2.5 \\ 1.65, & 2.5 < L^*_c < 4.3 \\ 1.8, & L^*_c > 4.3 \end{cases} \tag{51}$$

Finally, the critical pressure rise can be correlated with L^*_c. The reason is that the critical (i.e., maximum-allowable) separation scale is also related to the shock-reflection or expansion-wave regimes, which are affected by the cowl length. The data processed by Eqs. (50) and (51) are illustrated in Fig. 27b. In the logarithmic coordinate system, the data points fall onto two straight lines, indicating that the corrected pressure rise p^*_{uncM} exhibits exponential growth as L^*_c increases. An empirical formula can be obtained:

$$p^*_{\text{uncM}} = \begin{cases} \dfrac{L^{*1.66}_c}{2.4}, & 0 < L^*_c < 2.5 \\ \dfrac{L^{*3.35}_c}{9.6}, & L^*_c > 2.5 \end{cases} \tag{52}$$

The slope of short-cowl unstart significantly differs from the other two types, indicating that more shock reflection points lead to a higher growth rate of p^*_{uncM}, and the number of shock reflections has no significant effect on the growth rate of p^*_{uncM} when $n_t \geq 3$. The critical wall pressure data in the literature [26,32,33,36,37] accord with the empirical line roughly (Fig. 27b), despite that the literature data for the long-cowl unstart are rare. The self-similarity of p^*_{uncM} is clearly related to the separation length and shock reflection. More comprehensive verification and the underlying physical implications require further investigation.

It should be noted that the critical pressure rise in this paper is merely a derivative of the critical SWBLI flow. In contrast, for the straight duct (or isolator) unstart [79], the backpressure (related to the blockage ratio) dominates the SWBLI flow. The formation mechanisms and physical implications of the critical pressure are different. Hence, in the field of hypersonic inlets, unstarts induced by upstream geometric/aerodynamic parameters and backpressure are usually studied separately [14].

VI. Conclusions

In order to reveal the physical mechanisms and quantitative laws of unstart phenomena in two-dimensional contraction ducts in supersonic flow, the transition from started to unstarted states has been triggered by increasing the contraction angle under different Mach numbers, Reynolds numbers, entrance heights, and wedge lengths, and the unstart boundaries have been determined. By introducing the corrected cowl angle θ_{cM} and corrected internal contraction ratio ICR_{effM}, the existing unstart similarity laws are extended to different Mach numbers. The complete statement of the similarity law is as follows: if two contraction ducts share the same $(\theta_{\text{cM}}, L^*_c)$, $(\theta_{\text{cM}}, \text{ICR}_{\text{effM}})$, or $(L^*_c, \text{ICR}_{\text{effM}})$, their unstart characteristics are identical. Based on this, a universal empirical formula that agrees well with CFD results and literature data is established. The conversion relationships among the corrected internal contraction ratio ICR_{effM}, effective internal contraction ratio ICR_{eff}, and internal contraction ratio ICR are also obtained.

To reveal the physical significance of the generalized similarity law, theoretical models of critical flow structure are established for three unstart modes, and the quantitative unstart triggers are provided. The models are generalizable because of their self-similarity.

For the short-cowl unstart model, the free interaction theory is used to calculate the separation shock angle β_s. Empirical formulas related to the incoming Mach number, Reynolds number, and flow deflection angle are employed to calculate the separation length L_{sep} under the influence of expansion waves. The unstart trigger is that the projected height of the separation shock at the throat, $h_{\text{IO}'}$, increases to the effective throat height $h_{t\text{-inv}}$. The self-similarity of the short-cowl unstart boundary stems from the coupling between the cowl shock angle β_c and the separation region size.

The transitional unstart model considers the separation length L_{sep} that is not affected by expansion waves. It is assumed that unstart is triggered when the relative shock reflection spacing L_{24m}/L_{sep} reduces to a certain value. The unstart boundaries for the transitional mode are not strictly self-similar. The reason is that L_{24m}/L_{sep} depends on the relative entrance height $h_{t\text{-inv}}/\delta_c$, Mach number, and Reynolds number simultaneously, and it is independent of L_c within a certain range.

For the long-cowl unstart model, the shock-induced separation can be ignored, and instead, the shock reflections in the duct are considered. Unstart is triggered as the throat mass-averaged Mach number M_t drops to 1 or lower. M_t is self-similar only within a certain range of θ_{cM}.

Compared to the authors' previous research, this study establishes a theoretical foundation for the unstart similarity law. The empirical and theoretical prediction methods in this work are both applicable to engineering estimation, providing principles to the design and control of supersonic/hypersonic inlets. Besides, the extended similarity law for the critical wall pressure peak is given, which can serve as a supplementary criterion for inlet state monitoring. Strictly speaking, this paper establishes engineering models inspired by first principles since empirical corrections are made for SWBLI. The present work can be improved in the precise modeling of separation length coupled with expansion waves and shock reflection, dynamics of separation region growth, and three-dimensional flow effect. Moreover, it is meaningful to extend the nonreacting similarity law to the oblique detonation engine by considering chemical reactions.

Appendix A: Numerical Method Validation

To guarantee the reliability of the numerical method, the flowfields of shock-induced separation are simulated, and the results are compared to the wind tunnel experiments [80]. The physical model is shown in Fig. A1a, in which the shock impingement position is

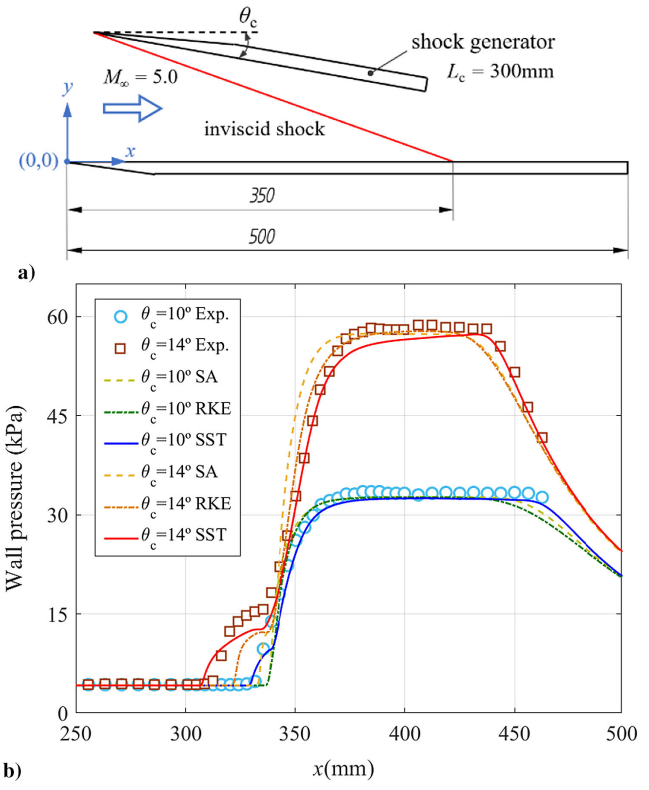

Fig. A1 Validation case for incident-shock-induced separation: a) schematic of physical model; b) wall pressure distribution.

fixed at $x = 350$ mm for different contraction angles θ_c. The incoming Mach number, static pressure, and static temperature are 5, 4007 Pa, and 68.3 K, respectively.

The applicability of three common turbulence models (Spalart-Allmaras (S-A), Realizable $k-\varepsilon$, and SST $k-\omega$) is examined. The pressure distributions on the lower wall are shown in Fig. A1b. The pressure curve obtained by the SST model shows a better coincidence with the experimental data than the S-A and Realizable $k-\varepsilon$ models, especially for the separation initiation point and pressure curve slopes. The other two models give a more conservative prediction of separation scale. Hence, the SST model is adopted in this paper. The validation results indicate that the numerical method is valid and appropriate.

Table B1 Unstart boundary obtained by experiments [22,26–29]

Reference	M_∞	θ_c, deg	α	θ_{cM}, deg	h_c, mm	ICR^{-1}	δ_c^*, mm	ICR_{eff}^{-1}	ICR_{effM}^{-1}
Cnossen	3.40	5.0	0.6	2.399	12.70	0.463	2.178	0.352	0.689
[22]	3.40	10.0	0.5	5.680	12.70	0.625	2.467	0.535	0.736
	4.90	5.0	0.6	1.927	12.70	0.251	2.540	0.064	0.639
	4.90	10.0	0.5	4.518	12.70	0.549	4.064	0.704	0.701
Emami	3.22	9.8	0.5	5.461	20.97	0.485	0.914	0.461	0.700
[26]	3.22	10.5	0.5	5.851	28.21	0.360	0.914	0.339	0.631
	3.22	10.0	0.5	5.723	29.57	0.344	0.914	0.323	0.623
	3.22	9.2	0.5	5.127	20.31	0.500	1.854	0.450	0.693
	3.22	9.1	0.5	5.071	25.83	0.393	1.854	0.346	0.636
	3.22	8.3	0.5	4.625	26.29	0.386	1.854	0.340	0.632
Van Wie	2.85	13.2	0.4	8.682	17.78	0.755	1.51	0.733	0.824
[27]	2.85	7.5	0.5	4.443	17.78	0.534	1.51	0.491	0.698
	2.85	10.6	0.4	6.972	12.70	0.724	1.51	0.687	0.794
	2.85	5.1	0.6	2.721	12.70	0.556	1.51	0.496	0.731
	2.85	6.2	0.6	3.307	7.62	0.550	1.51	0.439	0.701
	2.85	6.3	0.5	3.732	17.78	0.608	1.76	0.724	0.742
Li [28]	4.00	14.0	0.4	8.041	25.00	0.400	1.97	0.343	0.626
Jin [29]	2.47	13.0	0.4	9.055	24.16	0.513	0.72	0.498	0.650

Table B2 Unstart boundary obtained by numerical simulation [30–37]

Reference	M_∞	θ_c, deg	α	θ_{cM}, deg	h_c, mm	ICR^{-1}	δ_c^*, mm	ICR_{eff}^{-1}	ICR_{effM}^{-1}
Chang [30]	2.27	10.0	0.4	7.204	19.36	0.723	2.45	0.683	0.772
Fan [31]	2.51	7.0	0.5	4.422	17.05	0.645	2.66	0.579	0.736
Li [32]	2.49	14.0	0.4	9.713	15.30	0.654	1.59	0.613	0.732
Guo [33]	2.86	14.0	0.4	9.196	17.70	0.565	1.68	0.519	0.684
Su [34]	2.12	9.0	0.4	6.187	21.30	0.704	1.46	0.682	0.781
Reardon	3.22	9.8	0.5	5.461	29.18	0.348	0.880	0.328	0.625
[35]	3.22	11.0	0.5	6.130	31.49	0.322	0.880	0.304	0.611
Jin [36]	2.42	10.0	0.5	6.428	74.90	0.510	1.49	0.500	0.679
Yang [37]	2.14	10.0	0.5	6.836	23.989	0.714	1.88	0.690	0.787

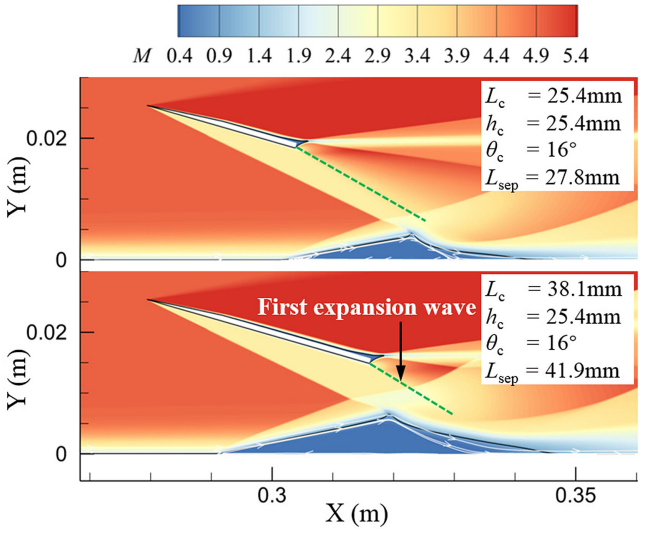

Fig. C1 Separation region affected by expansion waves ($M_\infty = 5$).

Appendix B: Unstart Boundary Data in the Literature

The unstart boundary data in the literature [22,26–37] are analyzed, including experimental and numerical results (Tables B1 and B2). This paper focuses on the unstart phenomena induced by varying Mach number, attack angle, or geometric configuration. The inlet unstart as a result of throat blockage or high backpressure is not considered because this kind of unstart is not dominated by upstream flow condition or duct configuration.

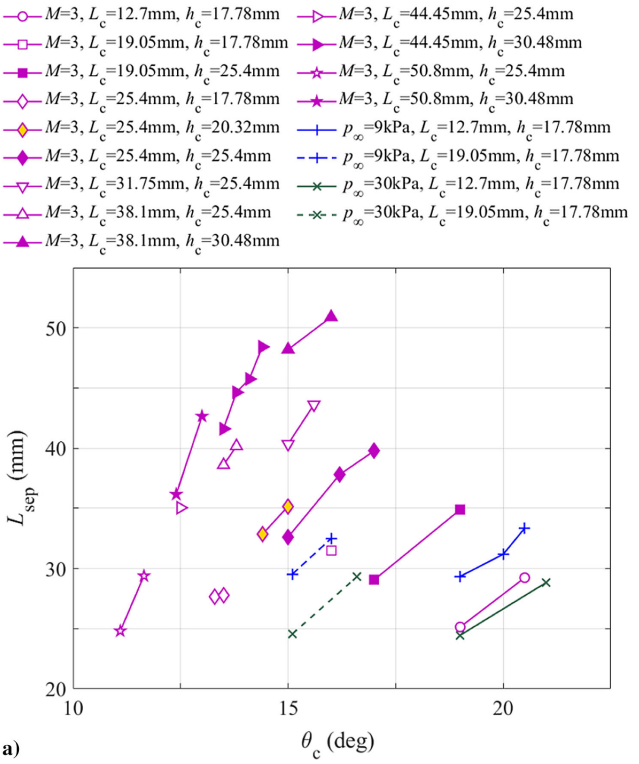

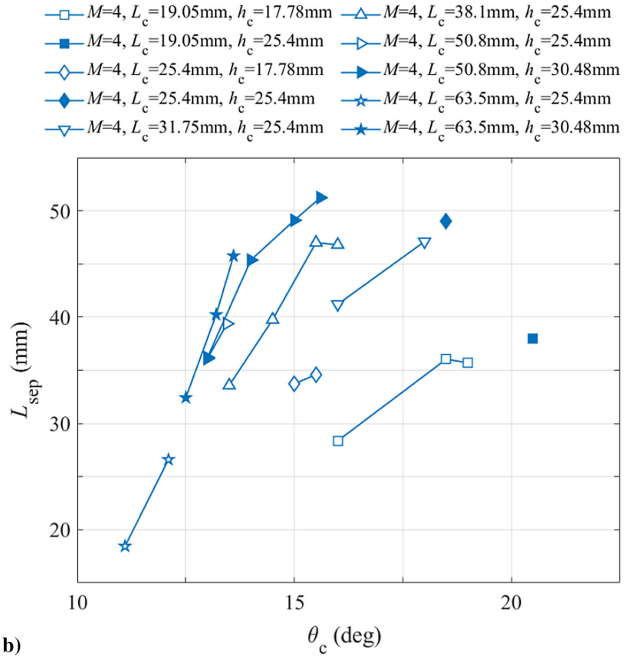

Fig. C2 Separation length varying with incoming flow condition and configuration: a) $M_\infty = 3$, b) $M_\infty = 4$, c) $M_\infty = 5$, and d) $M_\infty = 6$.

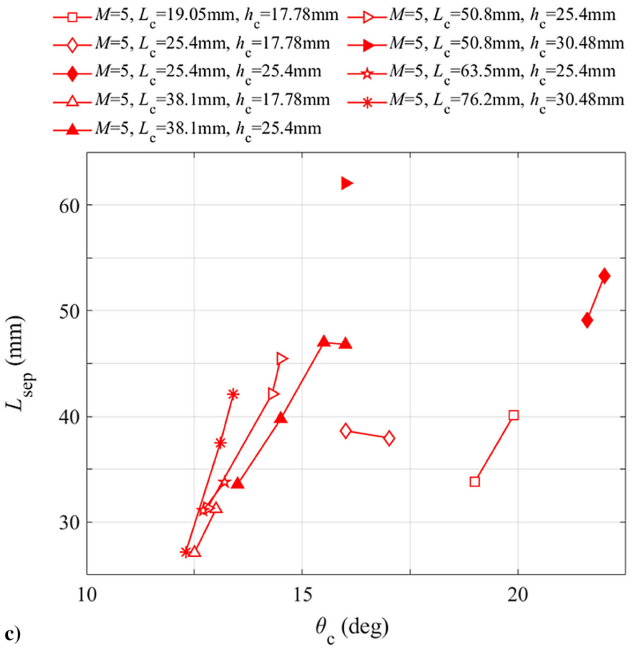

c)

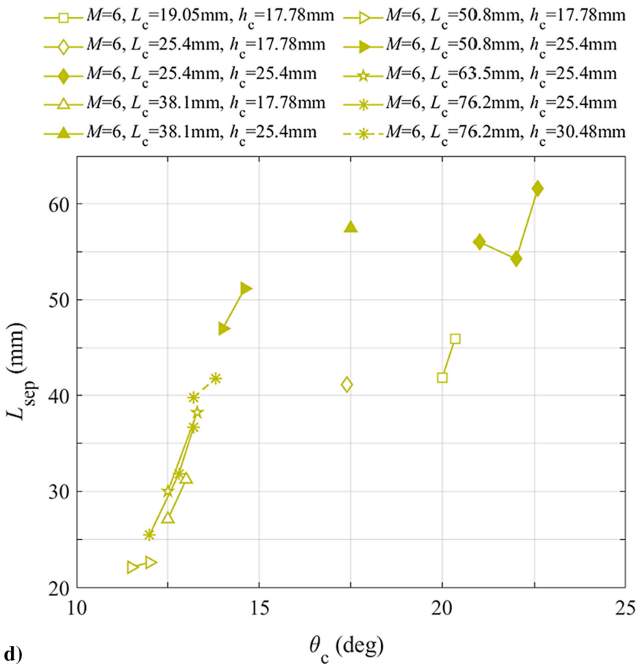

d)

Fig. C2 (Continued).

Appendix C: Separation Length Data

The separation length is affected significantly by the expansion waves from the wedge tail. As illustrated in Fig. C1, at the same incoming flow condition, the longer cowl plate causes a larger separation bubble because of the distanced expansion waves and incident shock wave. According to the numerical results, the separation length is measured under different flow conditions and expressed as functions of cowl length and cowl lip height, as shown in Fig. C2.

Acknowledgment

This work is sponsored by the National Natural Science Foundation of China (Nos. 12402383, U2141220, and 12372236).

References

[1] Anderson, J. D., *Modern Compressible Flow: With Historical Perspective*, 2nd ed., Mcgraw-Hill, New York, 1990, pp. 154–175.

[2] Heiser, W. H., Pratt, D. T., Daley, H. D., and Mehta, U. B., *Hypersonic Airbreathing Propulsion*, AIAA, Washington, D.C., 1994, pp. 197–267.

[3] Segal, C., *The Scramjet Engine-Processes and Characteristics*, Cambridge Univ. Press, New York, 2009, pp. 87–122.

[4] Van Wie, D. M., "Scramjet Inlets, Scramjet Propulsion," *Progress in Astronautics and Aeronautics*, edited by Paul Zarchan, AIAA, Reston, VA, 2001, pp. 447–511.

[5] Jiang, Z., "Standing Oblique Detonation for Hypersonic Propulsion," *A Review, Progress in Aerospace Sciences*, Vol. 143, 2023, Paper 100955.
https://doi.org/10.1016/j.paerosci.2023.100955

[6] Han, X., Liu, Y. F., Zhang, Z. J., Zhang, W. S., Yuan, C. K., Han, G. L., and Jiang, Z. L., "Experimental Demonstration of Forced Initiation of Kerosene Oblique Detonation by an On-Wedge Trip in an ODE Model," *Combustion and Flame*, Vol. 258, No. 113102, 2023, Paper 113102.
https://doi.org/10.1016/j.combustflame.2023.113102

[7] Zhang, Z. J., Liu, Y. F., and Wen, C. Y., "Mechanisms of the Destabilized Mach Reflection of Inviscid Oblique Detonation Waves before an Expansion Corner," *Journal of Fluid Mechanics*, Vol. 940, 2022, Paper A29.
https://doi.org/10.1017/jfm.2022.226

[8] Wang, K. L., Teng, H. H., Yang, P. F., and Ng, H. D., "Numerical Investigation of Flow Structures Resulting from the Interaction Between an Oblique Detonation Wave and an Upper Expansion Corner," *Journal of Fluid Mechanics*, Vol. 903, 2020, Paper A28.
https://doi.org/10.1017/jfm.2020.644

[9] Kumaran, R. M., Sundararajan, T., and Manohar, D. R., "Performance Evaluation of Second-Throat Diffuser for High-Altitude-Test Facility," *Journal of Propulsion and Power*, Vol. 26, No. 2, 2010, pp. 248–258.
https://doi.org/10.2514/1.43298

[10] Y., C., Jia, Z. Y., Li, W., and Ye, W. W., and Xu, "Numerical and Experimental Investigation of an Adjustable Dual-Channel Supersonic Diffuser," *Acta Astronautica*, Vol. 157, 2019, pp. 102–110.
https://doi.org/10.1016/j.actaastro.2018.12.017

[11] Yilmaz, C., McCormick, J., Carayon, A. B., Whitehead, B. E., Gabl, JR., and Pourpoint, T. L., "Design and Performance Evaluation of an Exhaust Diffuser for Altitude Testing of Chemical Rocket Engines," AIAA Paper 2020-3806, Aug. 2020.
https://doi.org/10.2514/MPEF20

[12] S., Y., Zhang, L., and Zhou, L. C., and Ji, "Investigation of Hysteresis Loop in the Starting Process of Supersonic Cascade," *AIAA Journal*, Vol. 60, No. 4, 2022, pp. 2685–2693.
https://doi.org/10.2514/1.J061232

[13] Czysz, PA., Bruno, C., and Chudoba, B., *Future Spacecraft Propulsion Systems and Integration: Technologies for Space Exploration*, 3rd ed., Springer-Verlag, Berlin, 2018, pp. 43–186.

[14] Chang, J. T., Li, N., Xu, K. J., Bao, W., and Yu, D. R., "Recent Research Progress on Unstart Mechanism, Detection and Control of Hypersonic Inlet," *Progress in Aerospace Sciences*, Vol. 89, 2017, pp. 1–22.
https://doi.org/10.1016/j.paerosci.2016.12.001

[15] Huang, H. X., Tan, H. J., Li, F. B., Tang, X. B., Qin, Y., Xie, L. B., Xu, Y. Y., Li, G. M., Gao, S. M., Zhang, Y., et al., "A Review of the Shock-Dominated Flow in a Hypersonic Inlet-Isolator," *Progress in Aerospace Sciences*, Vol. 143, No. 100952, 2023, Paper 100952.
https://doi.org/10.1016/j.paerosci.2023.100952

[16] Kantrowitz, A., and Donaldson, C., "Preliminary Investigation of Supersonic Differs," NACA WRL-713, 1945.

[17] Veillard, X., Tahir, R., Timofeev, E., and Mölder, S., "Limiting Contractions for Starting Simple Ramp-Type Scramjet Intakes with Overboard Spillage," *Journal of Propulsion and Power*, Vol. 24, No. 5, 2008, pp. 1042–1049.
https://doi.org/10.2514/1.34547

[18] Moradian, N., and Timofeev, E., "Starting Characteristics of Prandtl-Meyer Scramjet Intakes with Overboard Spillage," *Journal of Propulsion and Power*, Vol. 24, No. 5, 2018, pp. 189–197.
https://doi.org/10.2514/1.B36574

[19] Flock, A. K., and Gülhan, A., "Modified Kantrowitz Starting Criteria for Mixed Compression Supersonic Intakes," *AIAA Journal*, Vol. 57, No. 5, 2019, pp. 2011–2016.
https://doi.org/10.2514/1.J057283

[20] Janakiram, S., Kumar, G., Sinha, K., and Duvvuri, S., "Starting Characteristics of Curved Compression Ramp Air Intakes with Overboard Spillage," *AIAA Journal*, Vol. 62, No. 3, 2024, pp. 1066–1020.
https://doi.org/10.2514/1.J063281

[21] Cui, T., He, X. G., Yu, D. R., and Tang, S. L., "Multistability and Loops-Coupled Hysteresis: Flight-Test Analysis on Error Detection of

Inlet Start/Unstart," *Journal of Propulsion and Power*, Vol. 28, No. 3, 2012, pp. 496–503.
https://doi.org/10.2514/1.B34349

[22] Cnossen, J., and Obrien, R., "Investigation of the Diffusion Characteristics of Supersonic Streams Composed Mainly of Boundary Layers," AIAA Paper 1964-0245, June 1964.
https://doi.org/10.2514/6.1964-245

[23] Karanian, A. J., and Kepler, C. E., "Experimental Hypersonic Inlet Investigation with Application to Dual-Mode Scramjet," AIAA Paper 1965-0588, June 1965.
https://doi.org/10.2514/6.1965-588

[24] Air Force Aero-Propulsion Laboratory, "Hypersonic Ramjet Program for the Period 1 March to 31 December 1964, Vol. 1: 18-in. Engine Program," AFAPL-TR-65-36, 1965.

[25] McFarlin, D. J., and Kepler, C. A., "Mach 5 Test of Hydrogen-Fueled Variable Geometry Scramjet," AFAPL-TR-68-116, 1968.

[26] Van Wie, D. M., Kwok, F. T., and Walsh, R. F., "Starting Characteristics of Supersonic Inlets," AIAA Paper 1996-2914, July 1996.
https://doi.org/10.2514/6.1996-2914

[27] Emami, S., Trexler, C. A., Auslender, A. H., and Weidner, J. P., "Experimental Investigation of Inlet-Combustor Isolators for a Dual-Mode Scramjet at a Mach Number of 4," NASA TR 3502, 1995.

[28] Li, Z., Huang, B., Yang, J., Wei, Y., Liu, X., and Liu, J., "Starting Characteristics of Hypersonic Inlets in Shock Tunnel," *28th International Symposium on Shock Waves*, edited by K. Kontis, Springer, Berlin, 2012, pp. 1015–1020.
https://doi.org/10.1007/978-3-642-25685-1_154

[29] Jin, Y., Tan, H. J., Zhang, H., Zheng, G. J., Sun, S., and Zhang, Y., "Experimental Investigation on Unstart-Restart Hysteresis of a Supersonic Inlet During Throat Regulation," *Chinese Journal of Aeronaut*, Vol. 36, No. 11, 2023, pp. 135–152.
https://doi.org/10.1016/j.cja.2023.08.004

[30] Chang, J. T., Yu, D. R., Bao, W., Fan, Y., and Shen, Y., "Effects of Boundary-Layers Bleeding on Unstart/Restart Characteristics of Hypersonic Inlets," *Aeronautical Journal*, Vol. 113, No. 1143, 2009, pp. 319–327.
https://doi.org/10.1017/S0001924000002992

[31] Fan, Y., Chang, J. T., and Bao, W., "Effects of Wall Temperature on Unstart/Restart Characteristics of Hypersonic Inlet," *Journal of Solid Rocket Technology*, Vol. 32, No. 3, 2009, pp. 266–270.

[32] Li, Z. F., Gao, W. Z., and Yang, J. M., "Numerical and Experimental Investigation for Starting Characteristics of a Two-Dimensional Inlet," *Journal of Propulsion Technology*, Vol. 37, No. 7, 2016, pp. 1224–1232.

[33] Guo, S. T., Li, Z. F., Gao, W. Z., and Yang, J. M., "Analogy Between Effects of Attack Angle and Mach Number on Inlet Starting," *Journal of Propulsion Technology*, Vol. 38, No. 5, 2017, pp. 983–991.

[34] Chang, J. T., Yu, D. R., Bao, W., Fan, Y., and Shen, Y., "Effects of Boundary-Layers Bleeding on Unstart/Restart Characteristics of Hypersonic Inlets," *Aeronautical Journal*, Vol. 113, No. 1143, 2009, pp. 319–327.
https://doi.org/10.1017/S0001924000002992

[35] Reardon, J. P., Schetz, J. A., and Todd Lowe, K., "Computational Analysis of Unstart in Variable-Geometry Inlet," *Journal of Propulsion and Power*, Vol. 37, No. 4, 2021, pp. 564–576.
https://doi.org/10.2514/1.B38214

[36] Jin, Y., Sun, S., Tan, H. J., Zhang, Y., and Huang, H. X., "Flow Response Hysteresis of Throat Regulation Process of a Two-Dimensional Mixed-Compression Supersonic Inlet," *Chinese Journal of Aeronaut*, Vol. 35, No. 3, 2022, pp. 112–127.
https://doi.org/10.1016/j.cja.2021.06.013

[37] Yang, S. Z., Liao, K., Xie, W. Z., Yue, Y. J., Yang, L. L., and Guo, S. M., "Mechanisms of Hysteresis in the Acceleration and Deceleration Processes of Hypersonic Inlets," *Journal of Aerospace Engineering*, Vol. 36, No. 3, 2023, Paper 04023007.
https://doi.org/10.1061/JAEEEZ.ASENG-4645

[38] Babinsky, H., and Harvey, J. K., *Shock Wave-Boundary-Layer Interactions*, Cambridge Univ. Press, New York, 2011, Chaps. 2, 3.

[39] Goldberg, T. J., and Hefner, J. N., "Starting Phenomena for Hypersonic Inlets with Thick Turbulent Boundary Layers at Mach 6," NASA TN-D-6280, 1971.

[40] Yue, L. J., Jia, Y. N., Xu, X., Zhang, X. Y., and Zhang, P., "Effect of Cowl Shock on Restart Characteristics of Simple Ramp Type Hypersonic Inlets with Thin Boundary Layers," *Aerospace Science and Technology*, Vol. 74, 2018, pp. 72–80.
https://doi.org/10.1016/j.ast.2017.12.018

[41] Ramprakash, A., and Muruganandam, T. M., "Experimental Study on Start/Unstart Behavior of Two Dimensional Mixed Compression Inlet by Cowl Actuation," AIAA Paper 2016-5072, July 2016.
https://doi.org/10.2514/6.2016-5072

[42] Xu, S. C., Wang, Y., Wang, Z. G., Fan, X. Q., and Xiong, B., "Experimental Investigations of Hypersonic Inlet Unstart/Restart Process and Hysteresis Phenomenon Caused by Angle of Attack," *Aerospace Science and Technology*, Vol. 126, No. 107621, 2022, Paper 107621.
https://doi.org/10.1016/j.ast.2022.107621

[43] Chang, J. T., Hu, Q. H., Yu, D. R., and Bao, W., "Classifier Utility Modeling and Analysis of Hypersonic Inlet Start/Unstart Considering Training Data Costs," *Acta Astronautica*, Vol. 69, No. 9-10, 2011, pp. 841–847.
https://doi.org/10.1016/j.actaastro.2011.05.035

[44] Wu, H., Zhao, Y. P., Yang, T. L., and Tan, H. J., "An Ensemble Radius Basis Function Network Based on Dynamic Time Warping for Real-Time Monitoring of Supersonic Inlet Flow Patterns," *Aerospace Science and Technology*, Vol. 111, No. 106551, 2021, Paper 106551.
https://doi.org/10.1016/j.ast.2021.106551

[45] Chang, J. T., Yu, D. R., Bao, W., and Qu, L., "Influence Factors of Unstart Boundary for Hypersonic Inlets," AIAA Paper 2008-4586, July 2008.
https://doi.org/10.2514/6.2008-4586

[46] Tong, X. T., Yue, L. J., Chen, H., Zhang, Q. F., and He, C. M., "Similarity Analysis on Two-Dimensional Hypersonic Inlets Unstart," *AIAA Journal*, Vol. 61, No. 2, 2023, pp. 555–572.
https://doi.org/10.2514/1.J061874

[47] Tong, X. T., Yue, L. J., and Chen, H., "Similarity Analysis for Two-Dimensional Hypersonic Inlets Restart," *AIAA Journal*, Vol. 61, No. 10, 2023, pp. 4230–4246.
https://doi.org/10.2514/1.J062529

[48] Lui, H. F. S., Ricciardi, T. R., Wolf, W. R., Braun, J., Rahbari, I., and Paniagua, G., "Unsteadiness of Shock-Boundary Layer Interactions in a Mach 2.0 Supersonic Turbine Cascade," *Physical Review Fluids*, Vol. 7, 2022, Paper 094602.
https://doi.org/10.1103/PhysRevFluids.7.094602

[49] Bhagwandin, V. A., "Numerical Prediction of Shock-Boundary Layer Interaction Between a Pair of Fins in Hypersonic Flow," AIAA Paper 2014-3337, June 2014.
https://doi.org/10.2514/6.2014-3337

[50] Tong, X. T., Yue, L. J., Wu, W. N., Zhang, Q. F., and Chen, H., "Self-Similar Unstart Characteristics of Supersonic Contraction Duct with an Expansion Corner," *Physics of Fluids*, Vol. 36, No. 016148, 2024, pp. 2024.
https://doi.org/10.1063/5.0180243

[51] Barenblatt, G. I., *Scaling*, Cambridge Univ. Press, Cambridge, England, U.K., 2003, pp. 69–93.

[52] Watanabe, R., Ishii, T., Hirono, Y., and Maruoka, H., "Data-Driven Discovery of Self-Similarity Using Neural Networks," *Physical Review E*, Vol. 111, 2025, Paper 024301.
https://doi.org/10.1103/PhysRevE.111.024301

[53] Glauert, H., "The Effect of Compressibility on the Lift of an Aerofoil, Proceedings of the Royal Society A: Mathematical," *Physical and Engineering Sciences*, Vol. 118, No. 779, 1928, pp. 113–119.
https://doi.org/10.1098/rspa.1928.0039

[54] Tsien, H. S., "Two-Dimensional Subsonic Flow of Compressible Fluids," *Journal of Aeronautical Sciences*, Vol. 6, No. 10, 1939, pp. 399–407.
https://doi.org/10.2514/8.916

[55] Von Karman, T., "Compressibility Effects in Aerodynamics," *Journal of Aeronautical Sciences*, Vol. 8, No. 9, 1941, pp. 337–356.
https://doi.org/10.2514/8.10737

[56] Sriram, R., and Jagadeesh, G., "Correlation for Length of Impinging Shock-Induced Large Separation Bubble at Hypersonic Speed," *AIAA Journal*, Vol. 53, No. 9, 2015, pp. 2771–2776.
https://doi.org/10.2514/1.J053271

[57] Narayanan, A. S., and Verma, S. B., "Experimental Investigation of a Mach 4 Shock-Wave Turbulent Boundary Layer Interaction Near an Expansion Corner," AIAA Paper 2015-0112, Jan. 2015.
https://doi.org/10.2514/6.2015-0112

[58] Benek, J. A., Suchyta, C. J., and Babinsky, H., "The Effect of Wind Tunnel Size on Incident Shock Boundary Layer Interaction Experiments," AIAA Paper 2013-0862, Jan. 2013.
https://doi.org/10.2514/6.2013-862

[59] Hohn, O. M., and Gülhan, A., "Experimental Investigation of Sidewall Compression and Internal Contraction in a Scramjet Inlet," *Journal of Propulsion and Power*, Vol. 33, No. 2, 2017, pp. 501–513.
https://doi.org/10.2514/1.B36054

[60] Liu, X., Wang, Y., and Liang, J. H., "Research on Effects of Aspect Ratio on Starting Characteristics of 2-D Hypersonic Inlet with Forward-Swept Sidewall," *Journal of Propulsion Technology*, Vol. 36, No. 4, 2015, pp. 2649–2652.

[61] Wang, Z. G., Zhao, Y. L., Zhao, Y. X., and Fan, X. Q., "Prediction of Massive Separation of Unstarted Inlet via Free-Interaction Theory," *AIAA Journal*, Vol. 53, No. 4, 2015, pp. 1108–1111. https://doi.org/10.2514/1.J053501

[62] Zhou, Y. Y., Zhao, Y. L., and Zhao, Y. X., "A Study on the Separation Length of Shock Wave/Turbulent Boundary Layer Interaction," *International Journal of Aerospace Engineering*, Vol. 2019, 2019, Paper 8323787. https://doi.org/10.1155/2019/8323787

[63] Kartzer, E., "On the Lengthscales of Laminar Shock/Boundary-Layer Interaction," *Journal of Fluid Mechanics*, Vol. 206, 1989, pp. 477–496. https://doi.org/10.1017/S0022112089002375

[64] Grossman, I. J., and Bruce, P. J. K., "Confinement Effects on Regular-Irregular Transition in Shock-Wave-Boundary-Layer Interactions," *Journal of Fluid Mechanics*, Vol. 853, 2018, pp. 171–204. https://doi.org/10.1017/jfm.2018.537

[65] Grossman, I. J., and Bruce, P. J. K., "Sidewall Gap Effects on Oblique Shock-Wave/Boundary-Layer Interactions," *AIAA Journal*, Vol. 57, No. 6, 2019, pp. 2649–2652. https://doi.org/10.2514/1.J057952

[66] Fan, X. H., Wang, G., Lin, J. Z., Yang, Y. G., and Tang, Z. G., "Effects of Expansion Waves on Incident Shock-Wave/Boundary-Layer Interactions in Hypersonic Flows," *Physics of Fluids*, Vol. 35, 2023, Paper 056121. https://doi.org/10.1063/5.0153391

[67] Huang, T. L., Yue, L. J., Ma, S. H., Zhang, Q. F., Zhang, P., and Chang, X. Y., "Numerical Investigation on Flow Nonuniformity Induced Hysteresis in Scramjet Isolator," *Chinese Journal of Aeronautics*, Vol. 33, No. 12, 2020, pp. 3176–3188. https://doi.org/10.1016/j.cja.2020.04.019

[68] Zhu, Z. Y., Zhao, Y. L., Zhao, Y. X., Wang, L. C., and Zhou, Y. Y., "Influence of Expansion Corner on the Interaction of Dual Separation Zones," *AIP Advances*, Vol. 12, 2022, Paper 125207. https://doi.org/10.1063/5.0123331

[69] Li, N., and Chang, J. T., "Hysteretic Behaviors of Separation-Shock Driven by Backpressure in Isolator with Incident Shocks," *AIAA Journal*, Vol. 59, No. 3, 2021, pp. 960–971. https://doi.org/10.2514/1.J059331

[70] Li, X., Tan, H.-J., Zhang, Y., Huang, H.-X., Guo, Y.-J., and Lin, Z.-K., "Flow Patterns of Dual-Incident Shock Waves/Turbulent Boundary Layer Interaction," *Journal of Visualization*, Vol. 23, No. 6, 2020, pp. 931–935. https://doi.org/10.1007/s12650-020-00679-2

[71] Li, X., Zhang, Y., Tan, H., Jin, Y., and Li, C., "Comparative Study on Single-Incident and Dual-Incident Shock Wave/Turbulent Boundary Layer Interactions with Identical Total Deflection Angle," *Journal of Fluid Mechanics*, Vol. 940, 2022, Paper A7. https://doi.org/10.1017/jfm.2022.211

[72] Li, X., Zhang, Y., Tan, H., Sun, S., Yu, H., Jin, Y., and Zhou, J., "Separation Length Scaling for Dual-Incident Shock Wave-Turbulent Boundary Layer Interactions with Different Shock Wave Distances," *Journal of Fluid Mechanics*, Vol. 960, 2023, Paper A9. https://doi.org/10.1017/jfm.2023.181

[73] Rodi, P. E., Emami, S., and Trexler, C. A., "Unsteady Pressure Behavior in a Ramjet/Scramjet Inlet," *Journal of Propulsion and Power*, Vol. 12, No. 3, 1996, pp. 486–493. https://doi.org/10.2514/3.24061

[74] Srikant, S., Wagner, J. L., Valdivia, A., Akella, MR., and Clemens, N., "Unstart Detection in a Simplified-Geometry Hypersonic Inlet-Isolator Flow," *Journal of Propulsion and Power*, Vol. 26, No. 5, 2010, pp. 1059–1071. https://doi.org/10.2514/1.46937

[75] Souverein, L. J., Bakker, P. G., and Dupont, P., "A Scaling Analysis for Turbulent Shock-Wave/Boundary-Layer Interactions," *Journal of Fluid Mechanics*, Vol. 714, 2013, pp. 505–535. https://doi.org/10.1017/jfm.2012.495

[76] Helm, C. M., and Martín, M. P., "Scaling of Hypersonic Shock/Turbulent Boundary Layer Interactions," *Physical Review Fluids*, Vol. 6, 2021, Paper 074607. https://doi.org/10.1103/PhysRevFluids.6.074607

[77] Hong, Y., Li, Z., and Yang, J., "Scaling of Interaction Lengths for Hypersonic Shock Wave/Turbulent Boundary Layer Interactions," *Chinese Journal of Aeronautics*, Vol. 34, No. 5, 2021, pp. 504–509. https://doi.org/10.1016/j.cja.2020.12.028

[78] Wang, C. P., Xue, L. S., and Cheng, K. M., "Application of the Minimum Entropy Production Principle to Shock Reflection Induced by Separation," *Journal of Fluid Mechanics*, Vol. 857, 2018, pp. 784–805. https://doi.org/10.1017/jfm.2018.762

[79] Waltrup, P., and Billig, F., "Structure of Shock Waves in Cylindrical Ducts," *AIAA Journal*, Vol. 11, No. 10, 1973, pp. 1404–1408. https://doi.org/10.2514/3.50600

[80] Schülein, E., "Skin-Friction and Heat Flux Measurements in Shock/Boundary-Layer Interaction Flows," *AIAA Journal*, Vol. 44, No. 8, 2006, pp. 1732–1741. https://doi.org/10.2514/1.15110

J. Edwards
Associate Editor